JOURNAL OF PETROLOGY | VOLUME 52 | NUMBER 11 | PAGES 2147–2185 | 2011 | doi:10.1093/petrology/egr042

The Magmatic to Hydrothermal Evolution of the Intrusive Mont Saint-Hilaire Complex: Insights into the Late-stage Evolution of Peralkaline Rocks

JULIAN SCHILLING[1], MICHAEL A. W. MARKS[1], THOMAS WENZEL[1], TORSTEN VENNEMANN[2], LÁSZLÓ HORVÁTH[3], PETER TARASSOFF[4], DORRIT E. JACOB[5] AND GREGOR MARKL[1]*

[1]MATHEMATISCH-NATURWISSENSCHAFTLICHE FAKULTÄT, FACHBEREICH GEOWISSENSCHAFTEN, UNIVERSITÄT TÜBINGEN, WILHELMSTRAßE 56, D-72074 TÜBINGEN, GERMANY

[2]INSTITUT DE MINÉRALOGIE ET GÉOCHIMIE, UNIVERSITÉ DE LAUSANNE, UNIL-FSH2, CH-1015 LAUSANNE, SWITZERLAND

[3]594 MAIN ROAD, HUDSON HEIGHTS, QC J0P 1J0, CANADA

[4]91 LAKESHORE ROAD, BEACONSFIELD, QC H9W 4H8, CANADA

[5]INSTITUT FÜR GEOWISSENSCHAFTEN & EARTH SYSTEM SCIENCE RESEARCH CENTRE, JOHANNES GUTENBERG-UNIVERSITÄT, JJ. BECHER-WEG 21, D-55128 MAINZ, GERMANY

RECEIVED FEBRUARY 23, 2011; ACCEPTED AUGUST 26, 2011

The Cretaceous Mont Saint-Hilaire complex (Quebec, Canada) comprises three major rock units that were emplaced in the following sequence: (I) gabbros; (II) diorites; (III) diverse partly agpaitic foid syenites. The major element compositions of the rock-forming minerals, age-corrected Nd and oxygen isotope data for mineral separates and trace element data of Fe–Mg silicates from the various lithologies imply a common source for all units. The distribution of the rare earth elements in clinopyroxene from the gabbros indicates an ocean island basalt type composition for the parental magma. Gabbros record temperatures of 1200 to 800°C, variable silica activities between 0·7 and 0·3, and f_{O2} *values between −0·5 and +0·7 (log* ΔFMQ*, where FMQ is fayalite–magnetite–quartz). The diorites crystallized under uniform* a_{SiO2} *(*$a_{SiO2} = 0{\cdot}4–0{\cdot}5$*) and more reduced* f_{O2} *conditions (log* $\Delta FMQ \sim -1$*) between ~1100 and ~800°C. Phase equilibria in various foid syenites indicate that silica activities decrease from 0·6–0·3 at ~1000°C to <0·3 at ~550°C. Release of an aqueous fluid during the transition to the hydrothermal stage caused* a_{SiO2} *to drop to very low values, which results from reduced* SiO_2 *solubilities in aqueous fluids compared with silicate melts. During the hydrothermal stage, high water activities stabilized zeolite-group minerals. Fluid inclusions record a complex post-magmatic history, which includes trapping of an aqueous fluid that unmixed from the restitic foid syenitic magma. Cogenetic aqueous and carbonic fluid inclusions reflect heterogeneous trapping of coexisting immiscible external fluids in the latest evolutionary stage. The O and C isotope characteristics of fluid-inclusion hosted* CO_2 *and late-stage carbonates imply that the surrounding limestones were the source of the external fluids. The mineral-rich syenitic rocks at Mont Saint-Hilaire evolved as follows: first, alkalis, high field strength and large ion lithophile elements were pre-enriched in the (late) magmatic and subsequent hydrothermal stages; second, percolation of external fluids in equilibrium with the carbonate host-rocks and mixing processes with internal fluids as well as fluid–rock interaction governed dissolution of pre-existing*

*Corresponding author. Telephone: +49 7071 29 72930. Fax: +49 7071 293060. E-mail: markl@uni-tuebingen.de

minerals, element transport and precipitation of mineral assemblages determined by locally variable parameters. It is this hydrothermal interplay between internal and external fluids that is responsible for the mineral wealth found at Mont Saint-Hilaire.

KEY WORDS: *Mont Saint-Hilaire; agpaite; mineral chemistry; phase petrology; late-stage processes*

INTRODUCTION

Peralkaline [molar $(Na + K)/Al > 1$] rocks (Ussing, 1912; Marks *et al.*, 2011) form a subordinate group of igneous rocks that have attracted considerable scientific and economic interest in recent years. Within the peralkaline rock group, agpaitic rocks incorporate the high field strength elements (HFSE; such as Zr, Hf, Nb, Ta, Y, REE) into complex Na–K–Ca silicates such as the eudialyte solid solution series and minerals such as rinkite, wöhlerite and rosenbuschite (Sørensen, 1992, 1997; Andersen *et al.*, 2010; Markl *et al.*, 2010; Marks *et al.*, 2011; Schilling *et al.*, 2011*b*). They are considered to represent the most evolved igneous rocks that form by differentiation of nephelinitic or alkali basaltic parent magmas (Kramm & Kogarko, 1994; Marks *et al.*, 2004*b*; Schilling *et al.*, 2011*b*). In some peralkaline plutonic complexes, less fractionated lithologies are also present (gabbros, diorites and monzonites) that predate the agpaitic foid syenites (Marks *et al.*, 2011, and references therein).

In agpaitic systems the HFSE can be strongly enriched and may form economically important ore deposits (e.g. Kogarko *et al.*, 1982; Kogarko, 1990; Allan, 1992; Sørensen, 1992, 1997). The large ion lithophile elements (LILE, Na, K, Rb, Sr, Ba, Cs) may also reach exceptionally high concentrations, resulting in the formation of exotic and elsewhere rare LILE-incorporating minerals such as Rb- and Cs-rich rasvumite, tugtupite or polylithionite (e.g. Sørensen *et al.*, 1971; Bailey *et al.*, 1993; Chakhmouradian *et al.*, 2007).

Agpaites crystallize over extended temperature intervals down to solidus temperatures of 400–500°C (e.g. Sood & Edgar, 1970; Sørensen, 1997); subsequent to the magmatic stage, hydrothermal remobilization and transport processes result in the formation of characteristic minerals and phase assemblages (e.g. Horváth & Gault, 1990; Boily & Willams-Jones, 1994; Salvi *et al.*, 2000; Markl & Baumgartner, 2002; Mitchell & Liferovich, 2006). The late-stage evolution of well-studied agpaites implies the following modes of alteration and late-stage evolutionary trends.

(1) Interaction with later intruded melt batches: heat and matter provided by subsequently intruding melt batches cause a highly reactive environment that favors element dissolution, transport and re-precipitation (e.g. North Qoroq: Coulson, 1997; Tamazeght: Schilling *et al.*, 2009).
(2) Cooling in a largely closed system: magmatic–hydrothermal systems evolving mostly under closed-system conditions record pH changes in the coexisting fluid phase by the formation of characteristic minerals and phase assemblages (e.g. Ilímaussaq: Markl & Baumgartner, 2002; Pilansberg: Mitchell & Liferovich, 2006).
(3) Infiltration of external fluids: large-scale or locally restricted infiltration of external fluids appears to be common during cooling and uplift of peralkaline rocks (e.g. Tamazeght: Salvi *et al.*, 2000; Schilling *et al.*, 2009; Ilímaussaq: Graser & Markl, 2008). During the hydrothermal stage the primary minerals can locally be destabilized. In such assemblages, zeolites and calcite volumetrically predominate (Liou, 1979; Schilling *et al.*, 2009; Renac *et al.*, 2010).

In this study, we have reconstructed the magmatic to hydrothermal evolution of the Mont Saint-Hilaire complex as one of the most prominent examples of a multi-stage alkaline complex with extremely large mineral diversity (>400 minerals, L. Horváth, unpublished data; Horváth & Gault, 1990; Wight & Chao, 1995; Sørensen, 1997). Based on major, minor and trace element mineral chemistry and the radiogenic and stable isotope characteristics of selected minerals, we derive a petrogenetic model for the variously fractionated rock types of Mont Saint-Hilaire. Additionally, we constrain the intensive parameters under which the late-stage mineral assemblages formed using fluid inclusion data and the C and O isotopic compositions of carbonate and silicate mineral separates to reconstruct the sources of the fluids responsible for their formation. Finally, we discuss the magmatic to hydrothermal evolution of Mont Saint-Hilaire and draw conclusions about the crystallization of alkaline magmatic rocks over their extended crystallization intervals and the subsequent hydrothermal stage.

Regional geology

Mont Saint-Hilaire, located *c.* 40 km east of Montreal (Quebec, Canada), is part of the Cretaceous alkaline province of the Monteregian Hills, which consists of a number of west–east-trending intrusive bodies and accompanying dikes and sills, all emplaced at shallow crustal levels (e.g. Adams, 1903; Stansfield, 1923; Gold, 1967; Philpotts, 1974). Eaton & Frederiksen (2007) have proposed that the Monteregian Hills, the White Mountains and the New England Seamounts (from west to east) are the near-surface expressions of the great Meteor hotspot, which is situated beneath the North American plate and the adjacent North Atlantic Ocean. Based on the

radiogenic isotope characteristics of the Monteregian Hills plutons, their parental magmas are inferred to have ocean island basalt (OIB) characteristics, derived by partial melting of a depleted mantle source (Eby, 1985; Foland *et al.*, 1988). The variability of rock types observed within the Monteregian Hills intrusive rocks is mostly related to variable degrees of partial melting of the mantle source and variable degrees of crustal contamination (Foland *et al.*, 1988). Mont Saint-Hilaire, one of the central intrusions of the Monteregian Hills, is composed of silica-saturated (i.e. quartz- and feldspathoid-free) and silica-undersaturated (i.e. feldspathoid-bearing) rock units.

The ~125 Ma (Gilbert & Foland, 1986) Mont Saint-Hilaire multiphase intrusive complex consists of a succession of gabbros, diorites and foid syenites. The complex is exposed over an area of 4 km × 4 km and in an artificial outcrop owing to quarrying in the northeastern part within the most evolved foid syenites, where a diversity of exotic and elsewhere rare minerals is found in the Mont Saint-Hilaire Quarry (>400 valid minerals: L. Horváth, unpublished data; Chao *et al.*, 1967; Horváth & Gault, 1990; Wight & Chao, 1995). Previous petrological studies on Mont Saint-Hilaire have been undertaken by O'Neill (1914), Gold (1963), Rajasekaran (1967), Greenwood & Edgar (1984), Currie *et al.* (1986), Currie (1989) and Schilling *et al.* (2011*a*); its isotope characteristics were studied by Gilbert (1985), Gilbert & Foland (1986) and Foland *et al.* (1988).

Petrography

Three major lithologies can be distinguished in the Mont Saint-Hilaire complex (Fig. 1), as follows.

(I) Medium-grained nepheline-free gabbroic rocks with rare olivine (Sunrise Suite; terminology after Currie *et al.*, 1986; Table 1) form the most primitive rock unit that locally displays magmatic layering. The magmatic assemblage is apatite + ilmenite + titanomagnetite + plagioclase + clinopyroxene + amphibole + rare biotite + rare olivine (Fig. 2a–c). The modal amount of plagioclase is highly variable and some samples are virtually free of clinopyroxene (Fig. 2b), whereas in others clinopyroxene strongly predominates over amphibole (Fig. 2c). Locally, Fe–Ti oxides are rimmed by biotite (Fig. 2c) and clinopyroxene is finely intergrown with amphibole. Accessory minerals are zircon and pyrrhotite.

(II) Nepheline- and olivine-bearing diorites (Pain de Sucre Suite) are texturally similar to the gabbros and characterized by the magmatic assemblage apatite + ilmenite + titanomagnetite + plagioclase + olivine + clinopyroxene ± nepheline + amphibole and minor biotite (Fig. 2d); accessory minerals are baddeleyite and pyrrhotite. Biotite and alkali feldspar may occur as late-stage phases (Schilling *et al.*, 2011*a*; Table 1).

(III) Texturally and mineralogically variable foid-bearing syenitic rocks (East Hill Suite; Table 1) include (III-i) fine-grained porphyritic foid syenites with phenocrysts of alkali feldspar, nepheline, sodalite, amphibole and clinopyroxene (Fig. 2e). The groundmass consists of dispersed aegirine needles, albite, sulfides, magnetite and ilmenite with apatite and pyrrhotite as accessory phases. This unit contains autoliths of earlier crystallized gabbros (I) and diorites (II). The sodalite-rich syenite (III-ii; also referred to as sodalite syenite) occurs as centimeter- to meter-sized inclusions in (III-i) and also forms a distinct unit. It consists predominantly of euhedral sodalite and nepheline, and subordinate amphibole and clinopyroxene that are embedded in exsolved, poikilitic alkali feldspar (Fig. 2f). Locally, (III-ii) completely lacks clinopyroxene, amphibole and mica and contains minerals of the astrophyllite and eudialyte groups as well as other HFSE-incorporating phases. Felsic medium-grained foid syenites (III-iii) crystallized the assemblage alkali feldspar + nepheline + sodalite + clinopyroxene + biotite (Fig. 2g). Magnetite, pyrrhotite, titanite and eudialyte are accessory phases, although titanite and eudialyte do not occur together. Coarse- to very coarse-grained foid syenite (III-iv, 'igneous breccia': Horváth & Gault, 1990; Piilonen *et al.*, 1998) is composed of alkali feldspar, nepheline and clinopyroxene, and minor amphibole and sodalite and HFSE- and LILE-incorporating minerals (Fig. 2h). This unit contains numerous gabbroic and dioritic autoliths and xenoliths of marble and hornfels, which are rounded and digested to various degrees. In the contact zones of the groundmass with the various centimeter- to meter-scaled autoliths and xenoliths, characteristic mineral successions involving exotic and elsewhere rare phases have formed (see e.g. Horváth & Gault, 1990; Wight & Chao, 1995; Piilonen *et al.*, 1998); interstices and vugs are locally filled by subhedral to euhedral crystals of carbonates, sulfides and silicates.

Late-stage mineral associations from various syenites display the following textures. Graphite is rarely found in late-stage assemblages of the foid syenites (Fig. 3a). Sodalite occurs as a primary magmatic phase (sodalite-I) and, locally, as sodalite-II replacing earlier nepheline. Nepheline and sodalite (-I and -II) are overgrown by natrolite and analcime, (Fig. 3b and c). Carbonate minerals such as rhodochrosite and sabinaite occur in apparent textural equilibrium with, or, more commonly, rim earlier formed minerals such as analcime

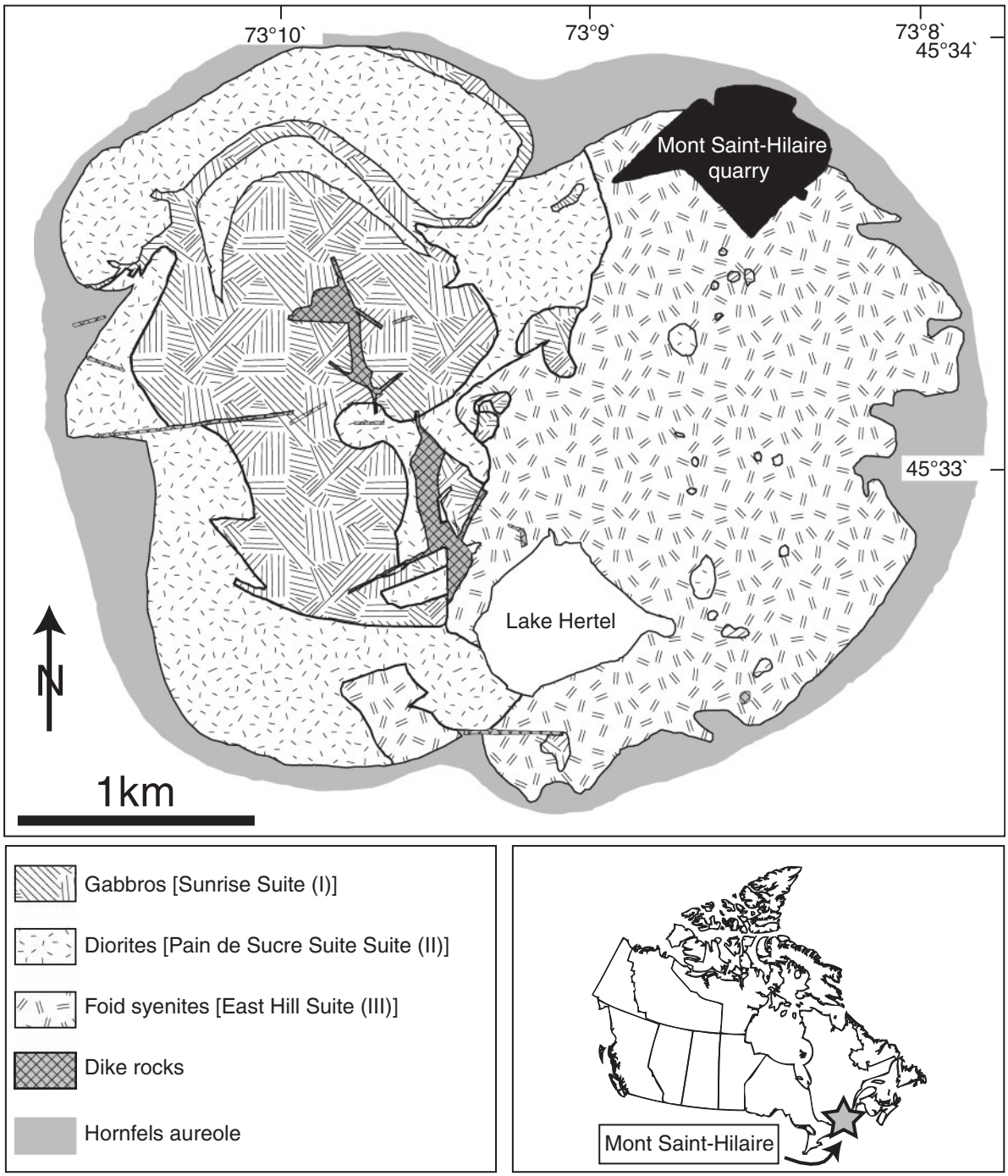

Fig. 1. Simplified geological map of the Mont Saint-Hilaire complex after Currie (1989). No further subdivision of the gabbro and diorite units can be undertaken owing to the poor outcrop in most parts of the complex. Sample coordinates are provided in the Electronic Appendix.

and natrolite (Fig. 3b–d). Zeolite-group minerals are locally associated with HFSE- and LILE-incorporating minerals such as eudialyte-group minerals (Fig. 3c). Primary magmatic alkali feldspar is albitized and sub-millimeter-sized laths of albite form veins and are in apparent textural equilibrium with analcime and natrolite. Locally, intergrowths of analcime with chabazite are observed (Fig. 3d). Cancrinite-group minerals, intergrown with analcime, locally undergo carbonatization.

Table 1: Summary of main characteristics of the Mont Saint-Hilaire lithologies

Rock type	Typical minerals	Important samples studied	Additional characteristics; figures
Gabbros (I; Sunrise Suite)	**Ap** + **Ilm** + **Mt** + **Plag** + **Cpx** + **Amp** ± Bt + Zrn + Po	MSH 17, 18, 80, 113, 115, 116, 120	Only MSH 113 ol-bearing; Fig. 2a–c
Diorites (II; Pain de Sucre Suite)	**Ap** + **Ilm** + **Mt** + **Plag** + **Cpx** + **Ol** + **Nph** + **Bt** + Bdy + Po	MSH 12, 14, 75, 119, 106b	Fig. 2d; see also Schilling *et al.* (2011*a*)
Foid syenites (III; East Hill Suite)			Subdivision based on field evidence, textures and mineral chemistry
Fine-grained porphyritic foid syenites (i)	Phenocrysts of **Afs** + **Nph** + **Cpx** + **Amp**; groundmass of **Aeg-rich Cpx** + **Ab** + **Sulfides** + **Ilm** + **Mt**	MSH 25, 37, 55, 67	MSH 55 and 37: late-stage veins in (i); (i) contains autoliths of (I), (II) and (ii) and host-rock xenoliths; Fig. 2e
Sodalite-rich foid syenite (ii)	Euhedral **Sdl** + **Nph**, poikilitic **Afs** + **Cpx** + **Amp**, HFSE- and LILE-incorporating minerals (e.g. EGM, AGM)	MSH 50, 54	In previous literature referred to as sodalite syenite; Fig. 2f
Medium-grained foid syenite (iii)	**Afs** + **Nph** + **Sdl** + **Cpx** + **Bt**	MSH 40, 90, 99, 105	Fig. 2g
Coarse-grained foid syenite (iv)	**Afs** + **Nph** + **Sdl** + **Cpx** + **Amp**, HFSE- and LILE-incorporating minerals (e.g. EGM, AGM)	MSH 28, 29, 51, 52, 59, 68	In previous literature referred to as igneous breccia owing to numerous autoliths and xenoliths; Fig. 2h
Late-stage assemblages in (III)	**Ab** + **Anl** + **Ntr** + **Cbz** + **Ccn** + **Or** + **various carbonates**	Samples beginning with T, LH, MOC, five-digit samples numbers, MSH 34	Late-stage assemblages found in all sub-units of (III); Fig. 3

Major constituents are in bold. Ilm, ilmenite; Mt, magnetite; Bdy, baddeleyite; Po, pyrrhotite; Ccn, cancrinite-group minerals; AGM, astrophyllite-group minerals. Other mineral abbreviations as in captions to Figs 2 and 3.

ANALYTICAL METHODS

Electron microprobe analyses

All mineral analyses were performed using a JEOL 8900 electron microprobe at the Fachbereich Geowissenschaften, Universität Tübingen, Germany. Major and minor elements were analyzed in wavelength-dispersive mode. For Fe–Mg and Na–Al silicates, the acceleration voltage was 15 kV with a beam current of 15 nA. Oxides were analyzed with an acceleration voltage of 20 kV and a beam current of 20 nA and carbonates were analyzed with an acceleration voltage of 15 kV and a beam current of 20 nA. Peak counting times were 16 s for major elements and 30–90 s for minor elements. Background counting times were half of the peak counting times. To avoid migration of Na in felsic minerals, we analyzed for Na first and used a defocused beam of 10 μm or where possible of 20 μm. Carbonates were analyzed with a defocused beam of 10 μm. For calibration, both synthetic and natural standards were used. Processing of the raw data was carried out with the internal ϕρz correction method of JEOL (Armstrong, 1991).

Bulk compositions of coarsely exsolved titanomagnetites and alkali feldspar were reconstructed by image processing (using the NIH ImageJ software) of back-scattered electron (BSE) images of the exsolved lamellae and host. Bulk compositions were calculated on the basis of the area proportions of the exsolved phases. Molar volumes of 44·52, 31·69, 100·07 and 108·72 cm^3 mol^{-1} were used for magnetite, ilmenite, albite and orthoclase, respectively (Robie & Hemingway, 1995). If finely exsolved lamellae of ilmenite were too small, we used a defocused electron beam of 20 μm to analyze bulk compositions. The full electron probe microanalysis (EPMA) dataset is provided as Supplementary Data in the Electronic Appendix (available for downloading at http://petrology.oxfordjournals.org/).

Laser ablation inductively coupled plasma mass spectrometry (LA-ICP-MS)

Trace elements were analyzed *in situ* with an Agilent 7500ce Quadrupole ICP-MS system coupled to a New Wave Research Merchantek UP-213 laser unit (Nd:YAG laser, output wavelength 213 nm) at the Institut für Geowissenschaften der Universität Mainz, Germany, following the procedure of Jacob (2006). Helium was used as the carrier gas and material was ablated with variable spot sizes between 55 and 100 μm with average pulse energy between 0·2 and 0·3 mJ per pulse and pulse

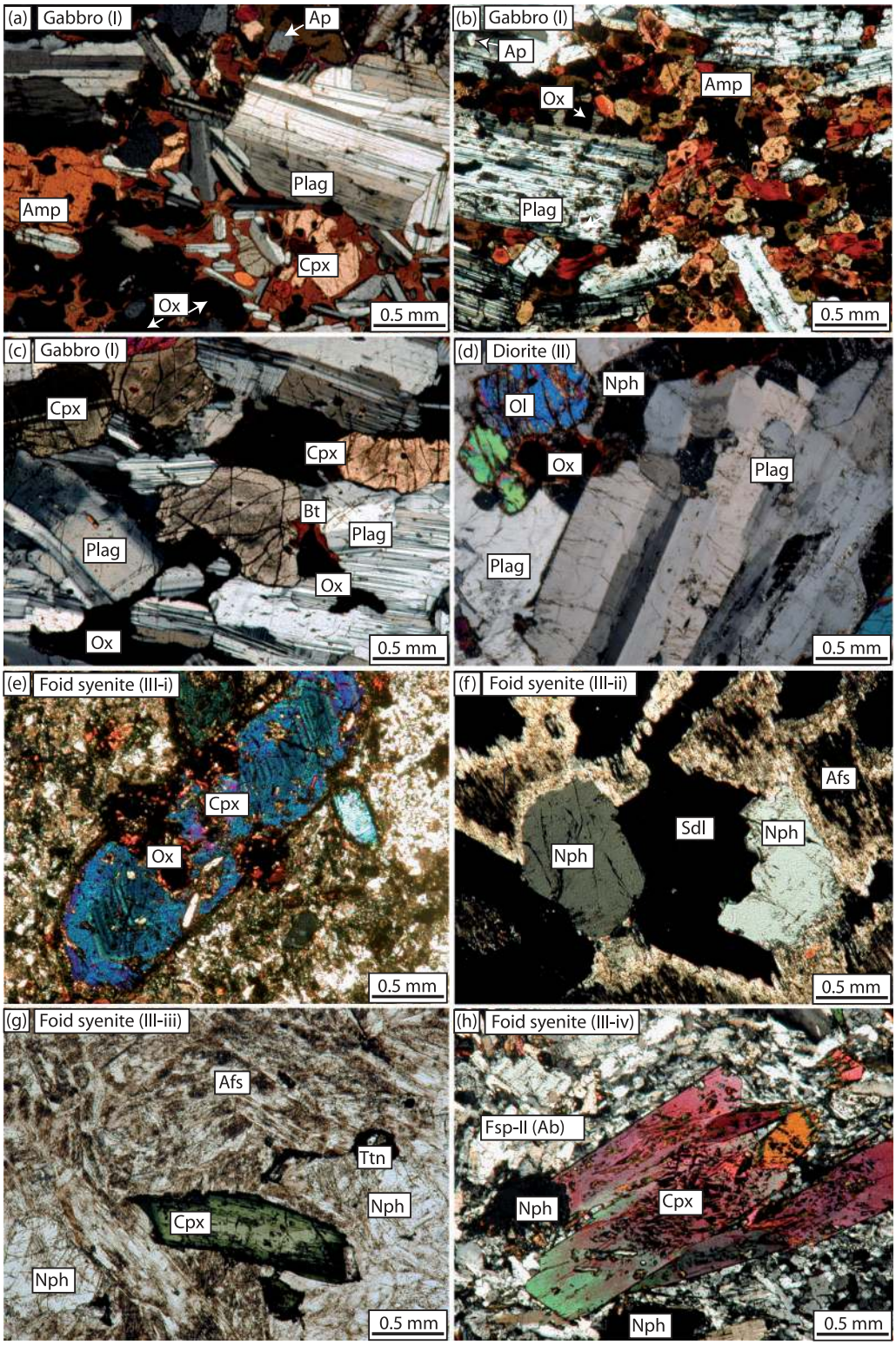

Fig. 2. Photomicrographs showing the characteristic textures of the major lithologies: (a), (b) and (c) represent textural varieties of the gabbros; (a) apatite, Fe–Ti oxides, plagioclase and clinopyroxene embedded in poikilitic amphibole; (b) apatite, Fe–Ti oxides and plagioclase coexisting with amphibole; (c) Fe–Ti oxides and plagioclase intergrown with clinopyroxene showing rutile exsolution; (d) orthomagmatic texture showing Fe–Ti oxides, olivine, nepheline and plagioclase in a diorite; (e) phenocryst of clinopyroxene with inclusions of Fe–Ti oxides in a fine-grained groundmass in foid syenite (III-i); (f) euhedral sodalite and nepheline embedded in poikilitic and exsolved alkali feldspar in sodalite-rich syenite (III-ii); (g) primary zoned clinopyroxene coexisting with alkali feldspar, nepheline and titanite in medium-grained foid syenite (III-iii); (h) clinopyroxene, nepheline and late-magmatic albite in coarse-grained foid syenite (III-iv). Ab, albite; Afs, alkali feldspar; Amp, amphibole; Ap, apatite; Bt, biotite; Cpx, clinopyroxene; Nph, nepheline; Ol, olivine; Ox, Fe–Ti oxide; Sdl, sodalite; Ttn, titanite; mineral abbreviations after Whitney & Evans (2010).

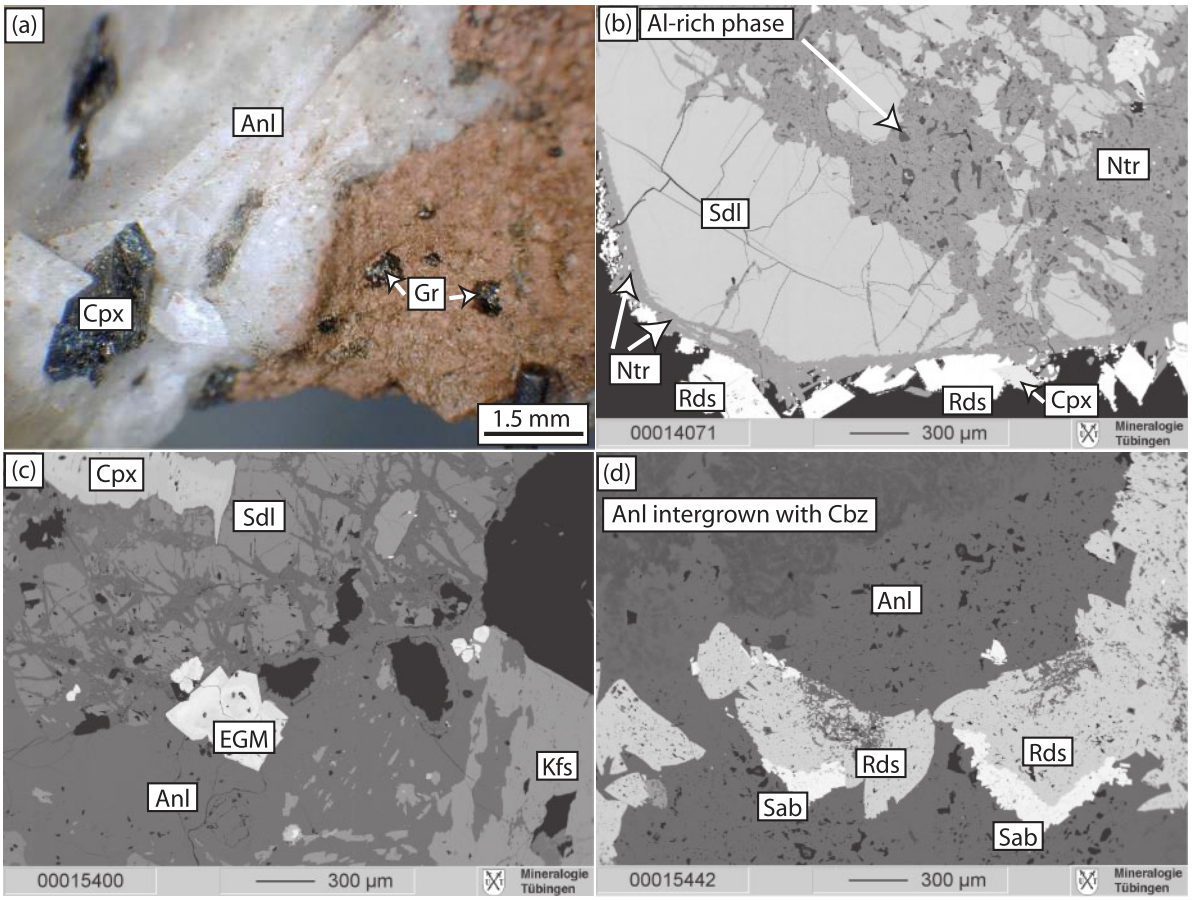

Fig. 3. Textures observed in late-stage assemblages of the foid syenites of Mont Saint-Hilaire. (a) Graphite (Gr) embedded in unidentified matrix surrounding clinopyroxene (Cpx) and analcime (Anl). (b) Relict sodalite (Sdl) rimmed and replaced by natrolite (Ntr), which locally is intergrown with an Al-rich phase; rhodochrosite (Rds) and clinopyroxene are interpreted to predate natrolitization; back-scattered electron (BSE) image. (c) Relict sodalite and K-feldspar and analcime. Clinopyroxene and eudialyte-group minerals (EGM) are in textural equilibrium with analcime; BSE image. (d) Analcime is locally intergrown with Na-chabazite (Cbz) and associated with sabinaite (Sab) and rhodochrosite (BSE image).

frequencies of 5 Hz for analyses on thin sections and of 10 Hz for analyses of Fe–Mg silicates embedded in epoxy disks. Each analysis consisted of 60 s background followed by 75 s ablation time (10 ms per peak and isotope, except for Sm and Nd, which were analyzed for 30 ms per peak and isotope). ^{28}Si was used as an internal standard with Si concentrations determined by EPMA. The NIST SRM 612 glass served as an external standard and USGS BCR2-G was analyzed as an unknown using Si concentrations listed in the GeoReM (http://georem.mpch-mainz.gwdg.de/) database (see Jochum & Nohl, 2008). For data processing we used the commercial GLITTER software (version 4.4.2; Macquarie University, Griffin *et al.*, 2008). Detection limits for most trace elements are <0·1 ppm, except for B, Ti, Cr and Zn, for which the detection limit is <1 ppm. P has a detection limit of ~3 ppm. Accuracy (1σ) based on the analyses of the BCR standard, which was analyzed at least every 15 analyses, is within ±10% for most elements (including the REE) and ±12 for B and Sc, ±16% for Ti, ±24% for Cu and ±50% for Sn (see Electronic Appendix).

Microthermometry and Raman spectroscopy of fluid inclusions

Microthermometry of fluid inclusions was carried out on a Linkam THMS 600 heating–freezing stage connected to a Leica polarizing microscope at the Fachbereich Geowissenschaften, Universität Tübingen. We used the triple point of CO_2 (−56·6°C), the melting point of H_2O (0·01°C), and the critical point of H_2O (374°C) of synthetic fluid inclusions for calibration. The reproducibility of final melting and homogenization temperatures were ±0·2 and ±2°C, respectively.

Qualitative Raman spectroscopic analyses were performed on a Dilor Labram laser–Raman spectrometer at the Fachbereich Geowissenschaften, Universität Tübingen.

For calibration, we used the spectra of calcite (1085 cm^{-1}) and crystalline silicon (520·7 cm^{-1}). The laser was operated at 11 mW at a wavelength of 488 nm. We collected spectra of vapor and liquid phases of the fluid inclusions from 400 to 5000 cm^{-1}.

Stable oxgyen isotopes of silicate minerals

The oxygen isotopic composition of ~10 mg hand-picked silicate material was analyzed on a Finnigan MAT 252 mass spectrometer following the methods of Sharp (1990) and Rumble & Hoering (1994), as described by Marks *et al.* (2003).

Stable carbon and oxygen isotopes of carbonates

Orthophosphoric acid (100%) was added to ~100–200 mg of pure and clean carbonate sample material in a ThermoFinnigan Gasbench II and the released CO_2 was transported via a He stream through a gas chromatograph directly into a Finnigan MAT 252 mass spectrometer (Spötl & Vennemann, 2003). As fractionation coefficients for orthophosphoric acid are unknown for some of the carbonates listed later in the paper, acid fractionation coefficients for calcite were used, which results in estimated larger errors of up to 1‰ for the respective carbonates. Error bars account for these errors in the respective figure.

Stable carbon and oxygen isotopes of fluid inclusion-extracted CO_2

C and O stable isotope compositions of CO_2 entrapped in fluid inclusions were analyzed on a Finnigan MAT 252 mass spectrometer. After checking suitable sample material containing CO_2-rich fluid inclusions qualitatively for CH_4 by Raman spectroscopy, samples containing methane-free fluid inclusions were mechanically crushed and the extracted fluid was introduced into a vacuum extraction line following the methods of Friedman (1953), Craig (1961), Vennemann & O'Neil (1993) and Köhler *et al.* (2008) and then analyzed on a Finnigan MAT 252 mass spectrometer.

Stable hydrogen isotopes of hydrosilicates

Measurements of the hydrogen isotope compositions of minerals were made using high-temperature (1450°C) reduction methods with He-carrier gas and a temperature conversion elemental analyzer linked to a Delta Plus XL mass spectrometer (Thermo-Finnigan) on 2–4 mg samples according to a method adapted from Sharp *et al.* (2001). The precision of the in-house kaolinite and G1 biotite standards for hydrogen isotope analyses was better than ±2‰ for the method used; all values were normalized using a value of −125‰ for the kaolinite standard and −65‰ for NBS-30.

Stable isotope analyses presented here are reported as per mil relative to VSMOW (oxygen and hydrogen) and relative to VPDB (carbon). Analytical errors for $\delta^{18}O$ (silicates and carbonates) and $\delta^{13}C$ (carbonates) are ±0·2‰.

Radiogenic Nd isotopes

Concentrations of Nd and Sm were analyzed by LA-ICP MS (see above); average values of at least four analyses performed on pure and optically homogeneous mineral separates were used to calculate the $^{147}Sm/^{144}Nd$ ratios. Mineral separates (~20 to ~30 mg) from selected samples were hand-separated, cleaned, crushed and subsequently treated with 2·5M and 6·1M HCl, centrifuged, triple-washed and centrifuged after each washing procedure. The samples were then treated with HF and the extraction of Nd was carried out in quartz columns using 1·7 ml Teflon powder coated with HDEHP (di-ethyl hexyl phosphate) as cation exchange medium that equilibrated with 0·18 N HCl (Marks *et al.*, 2003). Isotopes of Nd were analyzed by thermal ionization mass spectrometry (TIMS) on a Finnigan MAT 262 system in static collection mode on a Re double-filament configuration. $^{143}Nd/^{144}Nd$ isotope ratios were normalized to $^{146}Nd/^{144}Nd = 0{\cdot}7219$. The La Jolla Nd standard yielded a $^{143}Nd/^{144}Nd$ value of $0{\cdot}511919 \pm 0{\cdot}000011$ (reference value 0·511850); we applied a factor of 0·000069 to correct for deviation of the La Jolla standard analyses relative to the reference value. Total procedural blanks (chemistry and loading) were <120 pg for Nd.

RESULTS

Mineral compositions

Fe–Ti oxides

Titanomagnetite is $Usp_{24–84}Mt_{12–65}$ in gabbros, $Usp_{59–81}Mt_{11–38}$ in diorites (Schilling *et al.*, 2011*a*) and $Usp_{1–45}Mag_{55–93}$ in syenites (Fig. 4 and Table 2). $Ilmenite_{ss}$ (where ss indicates solid solution) is $Ilm_{63–90}Hem_{3–18}Gk_{1–30}Pph_{1–8}$ in gabbros, $Ilm_{76–89}Hem_{2–6}Gk_{3–16}Pph_{3–5}$ in diorites (Schilling *et al.*, 2011*a*) and $Ilm_{33–79}Hem_3Gk_0Pph_{19–63}$ in a fine-grained porphyritic foid syenite (Fig. 4 and Table 2).

Clinopyroxene

Clinopyroxene forms early magmatic crystals in all lithologies and additionally occurs as hydrothermal fine-grained masses and needles in the syenites; consequently, clinopyroxene is highly variable in composition and X_{Fe} [$X_{Fe} = (Fe_{tot})/(Fe_{tot} + Mg)$] is 0·17–0·35, 0·22–0·41 and 0·28–1 in gabbros, diorites and syenites, respectively. In terms of endmember distribution, clinopyroxene is $Di_{21–79}Hed_{7–27}Aeg_{1–11}$ in gabbros, $Di_{49–69}Hed_{9–34}Aeg_{1–10}$ in diorites and $Di_{0–56}Hed_{1–49}Aeg_{2–90}$ in foid syenites

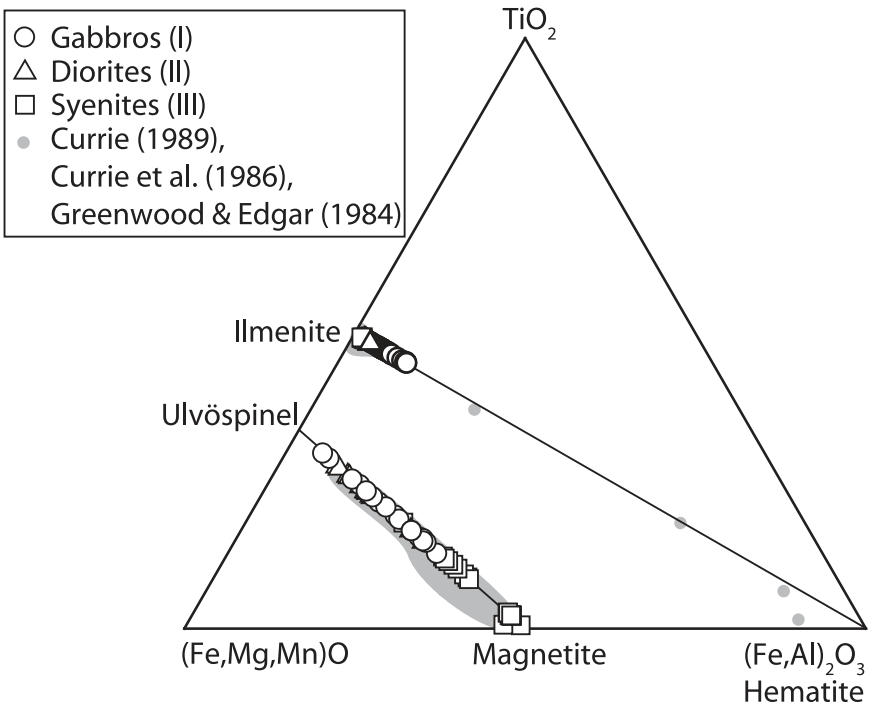

Fig. 4. Ternary plot [TiO_2–(Fe,Mg,Mn)O–$(Fe,Al)_2O_3$] showing the compositional variation of Fe–Ti oxides found in the various lithologies including data from Schilling *et al.* (2011*a*). Shown for comparison are the data of Greenwood & Edgar (1984), Currie *et al.* (1986) and Currie (1989).

(Fig. 5 and Table 3; see Mann *et al.*, 2006, for details on the calculation scheme for the pyroxene endmembers used). The jadeite component is ≤9 mol % in clinopyroxene of all units. Clinopyroxene is optically and chemically zoned (Fig. 2e and g) and we observed two zonation patterns in all units: sharp zonation patterns separating cores from rims are interpreted to be of primary origin whereas irregular zonations and overgrowths are of secondary origin and reflect late-stage (post-magmatic?) re-equilibration.

Olivine

Only one gabbroic sample (MSH 113) contains olivine ($Fo_{71–72}Fa_{27–28}Tep_1$). In diorites, olivine is $Fo_{28–64}Fa_{34–67}Tep_{1–5}$ (Schilling *et al.*, 2011*a*), whereas syenites lack olivine. No significant zonation is observed in olivine and variation of the various endmembers is ±3 mol % in olivine from all samples; Ca does not exceed 0·01 a.p.f.u. and Ni is below the detection limit of ~200 ppm (see Schilling *et al.*, 2011*a*).

Amphibole

Amphibole is a major phase in diorites, gabbros, fine-grained porphyritic foid syenites and sodalite-rich foid syenites, and rarely occurs in coarse-grained foid syenites. Two compositionally distinct groups of amphibole are recognized: amphibole from gabbros, diorites and core compositions of zoned crystals from syenites (III-I and III-iii) is calcic in composition (1·59–1·97 a.p.f.u. Ca) and ranges from kaersutite to magnesio-hastingsite (Mitchell, 1990; Leake *et al.*, 1997; Fig. 6, Table 4). Sodic amphibole (2·54–2·78 a.p.f.u. Na) forms slightly zoned crystals in sodalite-rich and coarse-grained foid syenites and rims calcic amphibole in fine-grained porphyritic foid syenites; sodic amphibole is arfvedsonite to ferric ferronyböite in composition (Leake *et al.*, 1997; Table 4) and generally occurs with highly evolved mineral assemblages such as aegirine-rich clinopyroxene, alkali feldspar, nepheline and sodalite. Calcic and sodic amphiboles are characterized by X_{Fe} values of 0·27–0·69 and 0·78–0·97, respectively. Ti is 0·24–0·76 a.p.f.u. in calcic amphibole and 0·06–0·28 a.p.f.u. in sodic varieties. Si is in the range of 5·82–6·8 a.p.f.u. and 7·36–7·91 a.p.f.u. in calcic and sodic amphiboles, respectively. Aluminum is 1·2–2·37 a.p.f.u. in calcic amphibole and 0·3–0·68 a.p.f.u. in sodic amphibole. Fluorine and chlorine are as high as 0·49 and 0·04 a.p.f.u., respectively.

Table 2: Representative compositions (wt %) of Fe–Ti oxides from Mont Saint-Hilaire

Sample:	MSH 17	MSH 115	MSH 17	MSH 115	MSH 105	MSH 99
	(I)	(I)	(I)	(I)	(III-iii)	(III-iii)
Analysis:	575–578 (reint)	614 (unexs)	568	613	345 (unexs)	341 (unexs)
TiO_2	15·85	16·43	46·40	47·98	8·15	1·49
FeO	77·52	72·44	48·19	47·53	78·91	84·70
MgO	0·19	2·58	1·44	0·36	0·02	0·00
MnO	0·75	0·88	1·88	1·52	4·31	4·57
Al_2O_3	0·53	3·42	0·03	0·07	0·16	0·19
SiO_2	0·17	b.d.l.	0·01	0·02	b.d.l.	0·01
ZnO	0·02	0·11	0·07	b.d.l.	0·48	0·37
Total	95·01	95·86	98·02	97·50	92·03	91·33
Formulae based on 3 cations and 4 O atoms (spinel-group minerals) and 2 cations and 3 O atoms (ilmenite-group minerals)						
Ferric form:	Ti–Mt	Ti–Mt	Ilm	Ilm	Mt	Mt
Ti	0·45	0·45	0·88	0·93	0·24	0·04
Fe^{2+}	1·43	1·28	0·79	0·88	1·08	0·88
Fe^{3+}	1·05	0·94	0·23	0·14	1·51	1·90
Mg	0·01	0·14	0·05	0·01	0·00	0·00
Mn	0·02	0·03	0·04	0·03	0·14	0·15
Al	0·02	0·15	0·00	0·00	0·01	0·01
Si	0·01	–	0·00	0·00	–	0·00
Zn	0·00	0·00	0·00	0·00	0·01	0·01
Ferric total	98·85	99·51	99·24	98·23	97·15	97·77
R^{2+}	1·46	1·45	0·88	0·93	1·23	1·03
R^{3+}	1·07	1·09	0·23	0·14	1·52	1·91
Ti^{4+}	0·45	0·45	0·88	0·93	0·24	0·04
X_{Usp}	0·45	0·45			0·24	0·04
X_{Ilm}			0·79	0·88		

Fe–Ti oxide analyses from diorites (II) have been given by Schilling *et al.* (2011*a*); X_{Usp} is endmember component of ulvöspinel in Ti–Mt; X_{Ilm} is endmember component in $Ilmenite_{solid\ solution}$; reint, reintegrated; unexs, unexsolved; b.d.l., below detection limit. ZrO_2 is below detection limit in all analyses.

Mica

Primary subhedral to interstitial trioctahedral Fe-rich dark mica is rare in gabbros and more common in diorites and syenites. Secondary biotite rimming Fe–Ti oxides is common in both gabbros and diorites and compositionally resembles primary biotite. X_{Fe} is 0·21–0·62 in gabbros, 0·33–0·62 in diorites and 0·39–0·99 in syenites. Titanium is in the range of 0·57–0·93 a.p.f.u. in gabbros, 0·21–0·99 a.p.f.u. in diorites and 0·08–0·46 a.p.f.u. in syenites (formulae normalized to 22 oxygens). As the sum of Si and Al is below eight in most analyses from gabbros and diorites, and, to a lesser degree also in syenites, some Fe^{3+} and/or Ti are assumed to be tetrahedrally coordinated, which is in agreement with compositional data for biotite from the gabbros and diorites (Greenwood & Edgar, 1984) and the Poudrette quarry (Lalonde *et al.*, 1996). The variation of Na is 0·08–0·22, 0·06–0·18 and 0·02–0·17 a.p.f.u. in biotite from gabbros, diorites and syenites, respectively. In biotite, potassium reaches 1·58–1·85 a.p.f.u. in gabbros, 1·67–1·88 a.p.f.u. in diorites and 1·76–2 a.p.f.u. in syenites. Chlorine and fluorine range between below detection limit and 0·08 a.p.f.u. (Cl) and 0·68 (F). With increasing degree of fractionation, mica evolves towards more annite-rich compositions.

Feldspar

Variably sized euhedral to subhedral $feldspar_{ss}$ is present in all rock types and pure albite laths occur in most late-stage

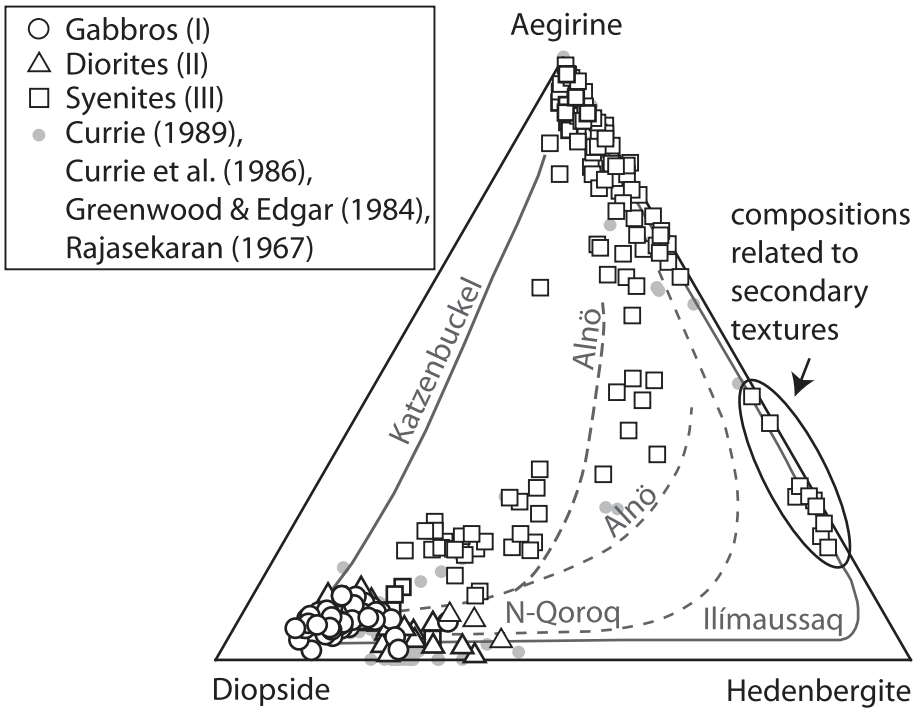

Fig. 5. Ternary plot showing clinopyroxene compositions in the system diopside–hedenbergite–aegirine. Dashed and continuous lines indicate the trends of data from other localities: Katzenbuckel (Mann *et al.*, 2006); Alnö (Vuorinen *et al.*, 2005); North Qoroq (Coulson, 2003); Ilímaussaq (Marks & Markl, 2001).

mineral associations in the syenites (Fig. 2f–h; Table 5). Plagioclase is optically and chemically zoned in some gabbros and diorites and X_{An}^{plag} decreases from core to rim. Plagioclase-rimming alkali feldspar is restricted to the diorites (Schilling *et al.*, 2011*a*). Primary alkali feldspar in syenites is perthitic in composition and only rarely do textures allow for reintegration; thus, most analyses reported represent exsolved lamellae (Fig. 7 and Table 5). In gabbros, plagioclase is $An_{37–86}Ab_{3–71}Or_{0–4}$ with up to 0·02 a.p.f.u. Sr. In diorites, plagioclase is $An_{52–13}Ab_{46–80}Or_{2–7}$ and alkali feldspar is $An_{3–14}Ab_{29–62}Or_{68–24}$ (Schilling *et al.*, 2011a). Alkali feldspar in the syenites compositionally covers the range $An_{0–10}Ab_{14–99}Or_{1–97}$ and Ba and Sr reach highest concentrations of 0·02 and 0·05 a.p.f.u., respectively (Table 5).

Nepheline and sodalite

Euhedral to subhedral nepheline in syenites is $Nph_{73–78}Kls_{14–23}An_1Qtz_{0–11}$ in molar proportions (Fig. 8, shown as wt % compositions; Table 6) and contains less Ca than nepheline from the diorites ($Nph_{69–75}Kls_{10–15}An_{7–9}Qtz_{4–10}$; Schilling *et al.*, 2011*a*). Fe (assumed as Fe^{3+}) reaches 0·08 a.p.f.u. No systematic differences are observed within the different foid syenitic lithologies and nepheline found in late-stage assemblages.

$Sodalite_{ss}$ closely resembles the sodalite endmember composition and Cl contents range from 1·68 to 1·98 a.p.f.u. Sulfur (S assumed as SO_3) ranges from 0·01 to 0·24 a.p.f.u. and the highest Cl/S ratios are observed in euhedral crystals from the sodalite-rich syenite (Table 6). Tetrahedrally coordinated Si, Al and Fe^{3+} vary in the range 5·92–6·11, 5·86–6·1 and 0–0·05 a.p.f.u., respectively, and sum close to the ideal value of 12 in most analyses. Sodalite found in late-stage assemblages associated with zeolite-group minerals has slightly higher contents of Al and slightly lower Si values than sodalite found in magmatic textures.

Zeolites

Analcime and natrolite are by far the most common zeolites found in the late-stage assemblages of the syenites. Analcime is characterized by analytical totals of 89–92 wt % and variable site occupancies of 1·92–2·08 a.p.f.u. Si, 0·9–1·06 a.p.f.u. Na and 0·92–1·09 a.p.f.u. Al (formulae normalized to six oxygens; Table 7). Natrolite has 2·97–3·06 a.p.f.u. Si, 1·84–1·99 a.p.f.u. Na and 1·97–2·03 a.p.f.u.

Table 3: Representative core and rim compositions (wt %) of clinopyroxene from Mont Saint-Hilaire

	core composition						rim composition	
Sample:	MSH 116	MSH 116	MSH 119	MSH 12	MSH 25	MSH 105	MSH 54	MSH 51
	(I)	(I)	(II)	(II)	(III-i)	(III-iii)	(III-ii)	(III-iv)
Analysis:	Cpx 6	Cpx 1	Cpx 4	Cpx 2	Cpx 3	Cpx 7	Cpx 4	Cpx 2
wt %								
SiO_2	46·09	46·64	49·32	50·58	40·21	50·41	51·99	51·73
Al_2O_3	6·44	6·05	3·69	3·28	14·20	1·58	0·70	0·74
FeO	6·91	7·21	8·60	7·85	10·36	15·22	26·94	27·65
MgO	12·70	12·84	12·98	13·11	7·06	7·22	0·54	0·07
MnO	0·10	0·13	0·40	0·41	0·22	2·47	1·25	1·28
TiO_2	2·76	2·86	2·06	1·63	4·48	0·63	0·34	0·07
ZrO_2	0·01	0·03	0·04	0·10	0·00	0·23	1·29	0·94
CaO	22·37	22·50	21·61	21·31	20·50	17·88	7·00	8·61
Na_2O	0·59	0·60	0·75	1·06	1·76	3·12	9·89	9·10
Total	97·97	98·85	99·46	99·31	98·79	98·77	99·95	100·18
Formulae based on 4 cations and 6 O								
Ferric form								
Si	1·74	1·75	1·85	1·89	1·53	1·95	1·98	1·98
Al	0·29	0·27	0·16	0·14	0·64	0·07	0·03	0·03
Fe^{3+}	0·11	0·11	0·08	0·06	0·17	0·23	0·66	0·64
Fe^{2+}	0·11	0·12	0·19	0·19	0·16	0·26	0·20	0·25
Mg	0·72	0·72	0·73	0·73	0·40	0·42	0·03	0·00
Mn	0·00	0·00	0·01	0·01	0·01	0·08	0·04	0·04
Ti	0·08	0·08	0·06	0·05	0·13	0·02	0·01	0·00
Zr	0·00	0·00	0·00	0·00	0·00	0·00	0·02	0·02
Ca	0·91	0·91	0·87	0·85	0·84	0·74	0·29	0·35
Na	0·04	0·04	0·05	0·08	0·13	0·23	0·73	0·68
Ferric total	98·36	99·24	99·73	99·52	99·40	99·55	102·27	102·39
X_{Fe}	0·24	0·24	0·27	0·25	0·45	0·54	0·97	1·00

K is below detection limit, except for MSH 119 Cpx 4 (0·02wt %), MSH 54 Cpx 4 (0·01wt %) and MSH 105 Cpx 7 (0·01wt %). Calculation of Fe^{3+} based on stoichiometry.

Al (formulae normalized to 10 oxygens; Table 7). Analytical totals of natrolite range from 87 to 91 wt %.

Carbonates

Carbonates are restricted to late-stage assemblages in syenites and occur as distinct crystals and fine-grained clots and masses. Most carbonates are solid solutions of calcite, rhodochrosite and siderite, and of the dolomite–ankerite series (Fig. 9, Table 8). Some carbonates contain significant amounts of REE, Zr, Ti, Na, and Al and were identified by EPMA and X-ray diffractometry (for details, see Horváth & Gault, 1990; Wight & Chao, 1995). The composition of the carbonate minerals is closely related to their texture: dolomite, rhodochrosite, siderite and complex HFSE-incorporating carbonates are intergrown with, or form rims around analcime and natrolite, whereas dawsonite and calcite form overgrowths and various replacement textures of earlier crystallized minerals. Hence, calcite and dawsonite are invariably the latest minerals to crystallize in late-stage environments.

Trace elements

We analyzed trace elements in clinopyroxene and amphibole from 14 representative samples (Fig. 10; Table 9) to investigate the genetic relationships between the various units and to characterize the composition of the potential parental melt. In gabbros, primitive mantle-normalized (Palme & O'Neill, 2004) REE patterns are concave-shaped

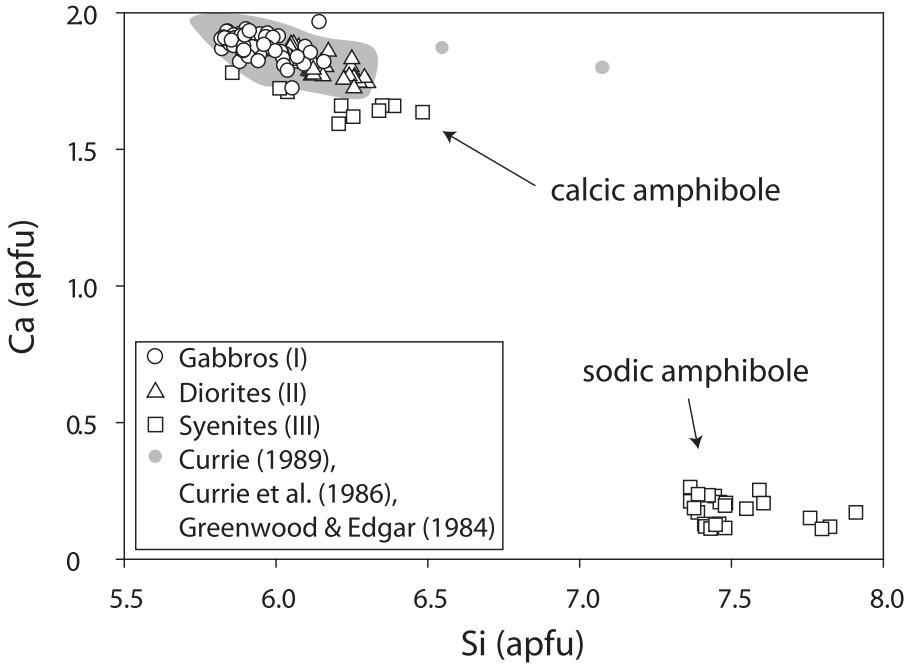

Fig. 6. Bivariate plot of Si vs Ca (a.p.f.u.) in amphibole. Calcic and sodic compositions form two compositionally distinct groups.

and the light REE (LREE) are enriched by factors of ~30 (clinopyroxene) to ~100 (amphibole), whereas the heavy REE (HREE) are less enriched by factors of ~10 (clinopyroxene) and ~50 (amphibole; Fig. 10a and b).

REE patterns of clinopyroxene and amphibole from diorites are subparallel compared with those of clinopyroxene and amphibole from gabbros, but are shifted to higher concentrations (Fig. 10a and b). Clinopyroxene and amphibole with the highest enrichments of REE have a slight negative Eu anomaly interpreted to result from the fractionation of plagioclase (which is evident from petrography in the gabbros and the diorites).

In syenites, the REE patterns of clinopyroxene vary with composition: in felsic medium-grained foid syenites (III-iii) and in clinopyroxene cores from fine-grained porphyritic (III-i) syenites, REE patterns resemble those of the diorites; whereas all REE patterns of clinopyroxene from the sodalite-rich syenite (III-ii), the coarse-grained foid syenite (III-iv) and Na–Fe^{3+}-rich compositions from (III-i) display pronounced negative Eu anomalies and are concave-shaped with the HREE being enriched to stronger degrees than the LREE (Fig. 10c). The concentration levels of the REE in clinopyroxene from (III-ii), (III-iv) and Na–Fe^{3+}-rich compositions from (III-i) are below or resemble those of clinopyroxene from the other syenitic units (Fig. 10c). The REE patterns of calcic amphibole from fine-grained porphyritic (III-i) syenites overlap with those of amphibole from diorites (Fig. 10d). REE patterns of Na–Fe^{3+}-rich amphibole from the sodalite-rich syenite (III-ii) are concave-shaped and characterized by a strong negative Eu anomaly and by equal or lower concentrations compared with the diorites (Fig. 10d). Thus, the REE distribution of clinopyroxene and amphibole from the various rock types may point to a continuous evolution from I to II and III.

The HFSE U, Th, Nb, Ta, Zr and Hf in most clinopyroxenes are enriched relative to primitive mantle, except for U and Th in some aegirine-rich compositions from the syenites where these elements are slightly depleted (Fig. 10a and c). Niobium and Ta are enriched by one to three orders of magnitude and the lowest concentrations are found in clinopyroxene from gabbros; Zr and Hf are enriched by one to four orders of magnitude and the highest concentrations were analyzed in aegirine-rich clinopyroxene from syenites (Fig. 10a and c). In amphiboles, Nb, Ta, Zr and Hf are invariably enriched; U and Th are either enriched or depleted in amphibole from the syenites (Fig. 10b and d). Niobium is invariably more enriched than Ta, whereas for Zr and Hf and for U and Th no systematic differences are observed in amphibole.

The LILE vary around the primitive mantle concentration level and Li displays negative anomalies in Ca-rich clinopyroxene. In contrast, positive Li anomalies are observed for aegirine-rich clinopyroxene from syenites. V is the only compatible element above the primitive mantle concentration level in clinopyroxene. Furthermore, negative anomalies are pronounced for Pb, Sr and Zn and a positive anomaly is observed for Sn. The LILE Rb, Sr

Table 4: Representative compositions (wt %) of amphibole from Mont Saint-Hilaire

Sample:	MSH 17	MSH 80	MSH 75	MSH 75	MSH 25	MSH 52	MSH 54
	(I)	(I)	(II)	(II)	(III-i)	(III-iv)	(III-ii)
Analysis:	A 2	Amp 137	A 1	Amp 14	A 1	Amp 237	A 2
SiO_2	40·12	40·29	41·37	40·47	38·79	46·44	47·01
TiO_2	6·50	4·36	6·57	4·39	5·62	1·33	1·35
Al_2O_3	12·11	11·52	10·66	11·08	13·30	3·42	3·31
FeO	10·47	13·40	10·78	15·03	13·74	30·06	30·38
MnO	0·31	0·55	0·27	0·47	0·35	3·48	2·97
MgO	12·66	11·01	12·41	10·19	10·44	0·53	1·59
CaO	11·48	11·39	11·44	11·04	11·01	0·73	1·11
Na_2O	3·15	2·74	3·07	2·86	3·27	8·94	8·91
K_2O	0·94	1·59	1·25	1·53	0·73	1·71	1·63
ZrO_2	0·01	0·08	0·12	0·15	0·03	0·33	0·93
Cl	0·02	0·04	0·01	0·05	0·03	0·00	0·00
F	0·00	0·17	b.d.l.	0·05	b.d.l.	0·51	0·00
Total	97·77	97·14	97·95	97·30	97·31	97·47	99·19
F–Cl = O	97·76	97·06	97·94	97·27	97·31	97·27	99·19
corrected							
Formulae based on 23 O, Fe^{3+} calculated after Schumacher (1997)							
	Ferrous	Ferrous	Ferrous	Ferrous	Ferrous	Ferric	Ferric
	form*	form*	form*	form*	form*	form†	form†
Si	5·94	6·11	6·12	6·16	5·86	7·45	7·38
Al	2·11	2·06	1·86	1·99	2·37	0·65	0·61
Ti	0·72	0·50	0·73	0·50	0·64	0·16	0·16
Mg	2·80	2·49	2·74	2·31	2·35	0·13	0·37
Fe^{2+}	1·30	1·70	1·33	1·91	1·73	3·15	3·17
Fe^{3+}						0·88	0·82
Mn	0·04	0·07	0·03	0·06	0·04	0·47	0·39
Ca	1·82	1·85	1·81	1·80	1·78	0·13	0·19
Na	0·90	0·81	0·88	0·84	0·96	2·78	2·71
K	0·18	0·31	0·24	0·30	0·14	0·35	0·33
Zr	0·00	0·01	0·01	0·01	–	0·03	0·07
Cl	0·00	0·01	0·00	0·01	0·01	0·00	0·00
F	0·00	0·08	–	0·02	0·00	0·26	0·00
Ferric total						97·91	100·24
X_{Fe}	0·32	0·41	0·33	0·45	0·42	0·97	0·91
amphibole	kaersutite	kaersutite	kaersutite	kaersutite	kaersutite	ferric	ferric
nomenclature						ferronyböite	ferronyböite

*Ferrous form is given because C-site is underoccupied and hence, no Fe^{3+} calculation is possible (Schumacher, 1997).
†Ferric iron can be calculated as the C-site is overoccupied and Fe^{3+} is calculated following table A-2 in appendix 2 of Leake *et al*. (1997) after the scheme of Schumacher (1997).
Amphibole nomenclature is from Leake *et al*. (1997).

Table 5: Representative compositions (wt %) of feldspar from Mont Saint-Hilaire

Sample:	MSH 115 (I)	MSH 17 (I)	MSH 90 (III-iii)	MSH 90 (III-iii)	MSH 99 (III-iii)	MSH 52 (III-iv)
Analysis:	Fsp 155	Fsp 292	Fsp 189	Fsp 186	Fsp 202–205 reint	Fsp 333–336 reint
SiO_2	48·76	54·38	65·80	69·71	68·08	67·70
Al_2O_3	32·29	28·39	17·56	18·66	18·31	18·68
Fe_2O_3	0·44	0·28	0·15	0·24	0·27	0·15
CaO	15·63	11·09	0·00	0·03	0·04	0·00
K_2O	0·09	0·38	16·45	0·17	3·56	6·43
Na_2O	2·28	4·82	0·50	11·83	9·16	7·02
BaO	0·01	0·03	b.d.l.	b.d.l.	0·03	b.d.l.
SrO	0·54	0·56	b.d.l.	b.d.l.	0·02	b.d.l.
Total	100·03	99·93	100·46	100·64	99·48	99·99
Formulae based on 8 O						
Si	2·24	2·47	3·03	3·03	3·02	3·02
Al	1·75	1·52	0·95	0·95	0·96	0·98
Fe^{3+}	0·02	0·01	0·01	0·01	0·01	0·00
Ca	0·77	0·54	0·00	0·00	0·00	0·00
K	0·01	0·02	0·97	0·01	0·20	0·37
Na	0·20	0·42	0·04	1·00	0·79	0·61
Ba	0·00	0·00	–	–	0·00	–
Sr	0·01	0·01	–	–	0·00	–
X_{An}	0·77	0·54	0·00	0·00	0·00	0·00
X_{Ab}	0·20	0·42	0·04	1·00	0·79	0·61
X_{Or}	0·01	0·02	0·97	0·01	0·20	0·37

Feldspar analyses from diorites (II) have been given by Schilling *et al.* (2011*a*); reint, reintegrated; b.d.l., below detection limit. X_{An}, X_{Ab} and X_{Or} are the endmember proportions of anorthite, albite and orthoclase, respectively.

and Pb are moderately enriched and their respective concentrations do not correlate with textural position or assemblage of the mineral analyzed in the various lithologies. In most Ca-rich clinopyroxene and amphibole compositions, Li is characterized by negative anomalies, whereas aegirine-rich compositions display positive anomalies of Li (Fig. 10). Except for V, the compatible elements Cr, Co, Ni and Cu are depleted or even below the detection limits of ~0·1 ppm in both clinopyroxene and amphibole.

Zr/Hf ratios of clinopyroxene vary from subchondritic [gabbros, diorites, fine-grained porphyritic (III-i) and felsic medium-grained (-iii) foid syenites] to superchondritic [sodalite-rich (III-ii) and coarse-grained (III-iv) foid syenites] values whereas Nb/Ta and U/Th ratios are invariably subchondritic and superchondritic, respectively (not shown). Except for one syenitic sample, the Y/Ho ratio of clinopyroxene is subchondritic. In amphibole, Zr/Hf is subchondritic in the gabbros and sub- to superchondritic in diorites and syenites. The Nb/Ta and U/Th ratios are chondritic in amphibole from gabbros and diorites and chondritic to superchondritic in syenites. Amphibole from gabbros and diorites is subchondritic with respect to Y/Ho, whereas amphibole from syenites is sub- to superchondritic in Y/Ho. Both clinopyroxene and amphibole overlap in their Zr/Hf, Nb/Ta, U/Th and Y/Ho ratios and do not show any offsets between the suites.

Radiogenic isotopes

Eleven separates of clinopyroxene and amphibole from all suites and sub-units were analyzed for their Sm–Nd characteristics and corrected for an age of 125 Ma (Gilbert & Foland, 1986) to constrain the source region and the petrogenetic relationships of the various lithologies; the respective $\varepsilon_{Nd}(T = 125\ Ma)$ values are sorted according to X_{Fe} in Fig. 11. The $\varepsilon_{Nd}(T = 125\ Ma)$ of clinopyroxene and amphibole varies from 4·7 to 5·7 in gabbros, from 4·8 to 5·2 in diorites and from 4·4 to 4·7 in primary magmatic syenites (Fig. 11, Table 10). Thus, most analyses from all units overlap within error with respect to their Nd isotopic composition.

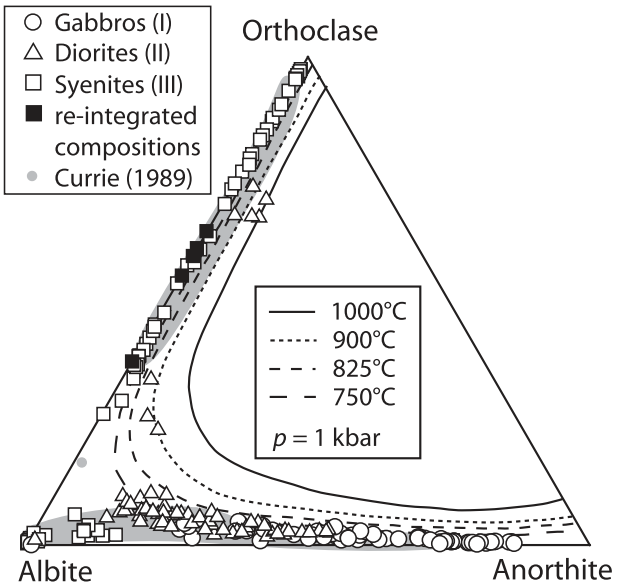

Fig. 7. Ternary plot showing feldspar compositions. Reintegrated compositions in syenites are represented by filled symbols. Isotherms for 1 kbar are taken from Fuhrman & Lindsley (1988), which are equivalent to the solvus limits for a pressure of 1 kbar that is assumed to correspond to the depth of emplacement of the Mont Saint-Hilaire intrusive complex (Currie *et al.*, 1986). Shaded fields represent the range of data from Currie (1989).

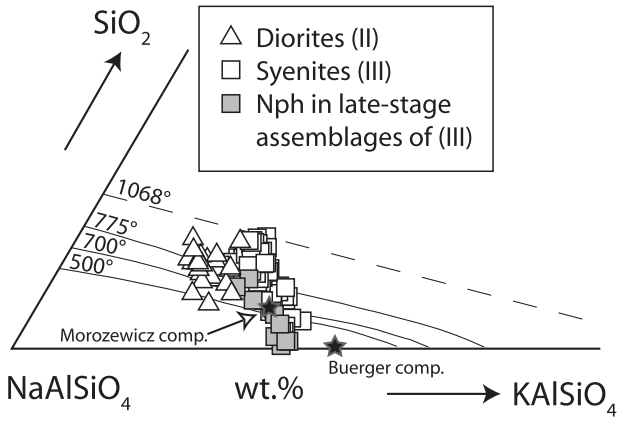

Fig. 8. Nepheline composition in the ternary system $NaAlSiO_4$–$KAlSiO_4$–SiO_2 (plotted as wt %). The Morozewicz and Buerger compositions (stars) are shown for comparison. Isotherms after Hamilton (1961). The nepheline compositions of Currie *et al.* (1986) overlap with the data presented here.

Table 6: Representative compositions (wt %) of nepheline and sodalite from syenites from Mont Saint-Hilaire

Sample:	MSH 90 (III-iii)	MSH 55 (III-i)	VMA 5	T234	VMA 6	MSH 105 (III-iii)	MSH 67 (III-i)	VMA 6
Analysis:	Nph 178	Nph 305	Nph 117	Nph 38	Nph 17	Sdl 72	Sdl 39	Sdl 137
SiO_2	46·34	44·30	42·16	46·85	43·19	37·71	37·20	35·91
Al_2O_3	31·23	32·82	34·16	31·51	34·14	31·00	30·86	31·13
Fe_2O_3	0·80	0·16	0·11	0·50	0·20	0·26	0·38	0·22
CaO	0·01	0·01	0·02	0·02	b.d.l.	0·03	0·05	0·01
Na_2O	16·41	15·93	16·29	15·95	16·36	24·33	24·69	25·28
K_2O	5·26	6·48	7·24	5·10	6·81	b.d.l.	0·05	0·03
Cl	b.d.l.	b.d.l.	b.d.l.	b.d.l.	b.d.l.	6·66	6·75	6·23
SO_3	b.d.l.	b.d.l.	b.d.l.	b.d.l.	b.d.l.	0·34	0·38	1·28
Total	100·05	99·70	99·97	99·93	100·70	100·33	100·37	100·10
	Nepheline formulae based on 16 O					*Sodalite formulae based on 21 O*		
Si	4·36	4·26	4·08	4·44	4·13	6·08	6·06	5·94
Al	3·60	3·72	3·90	3·52	3·85	5·89	5·92	6·07
Fe^{3+}	0·02	0·01	0·01	0·04	0·01	0·03	0·05	0·03
Ca	0·15	0·00	0·00	0·00	–	0·00	0·01	0·00
Na	2·90	2·97	3·06	2·93	3·04	7·60	7·79	8·11
K	0·48	0·79	0·89	0·62	0·83	–	0·01	0·01
Cl	–	–	–	–	–	1·82	1·86	1·75
S^{6+}	–	–	–	–	–	0·04	0·05	0·16

VMA 5, T234 and VMA 6 represent late-stage assemblages. Nepheline analyses from diorites (II) have been given by Schilling *et al.* (2011*a*).

Table 7: Representative compositions of zeolite-group minerals from late-stage assemblages from syenites from Mont Saint-Hilaire

Sample:	VMA 3	VMA 4	VMA 5	T645	T646	VMA 9
Analysis:	Anl 65	Anl 68	Anl 102	Ntr 228	Ntr 258	Ntr 29
SiO_2	54·58	55·59	50·83	45·01	47·90	47·37
Al_2O_3	23·25	22·28	24·28	26·14	26·72	26·69
Fe_2O_3	0·02	b.d.l.	0·19	0·09	0·03	0·07
CaO	0·01	b.d.l.	b.d.l.	0·02	0·01	0·01
Na_2O	13·89	13·13	14·33	15·51	15·81	15·50
K_2O	0·01	0·08	0·04	0·03	0·00	0·04
SrO	b.d.l.	b.d.l.	b.d.l.	b.d.l.	0·01	b.d.l.
BaO	0·02	0·03	0·01	0·01	0·01	0·01
SO_3	0·02	0·02	b.d.l.	0·02	b.d.l.	b.d.l.
Total	91·80	91·13	89·69	86·84	90·49	89·69
Formulae based on 6 O (analcime) and 10 O (natrolite)						
Si	2·00	2·04	1·92	2·97	3·02	3·02
Al	1·00	0·96	1·08	2·03	1·99	2·00
Fe^{3+}	0·00	–	0·01	0·00	0·00	0·00
Ca	0·00	–	–	0·00	0·00	0·00
Na	0·99	0·93	1·05	1·99	1·94	1·91
K	0·00	0·00	0·00	0·00	0·00	0·00
Sr	–	–	–	–	0·00	–
Ba	0·00	0·00	0·00	0·00	0·00	0·00
S^{6+}	0·00	0·00	–	0·00	–	–

Anl, analcime, Ntr, natrolite; b.d.l., below detection limit.

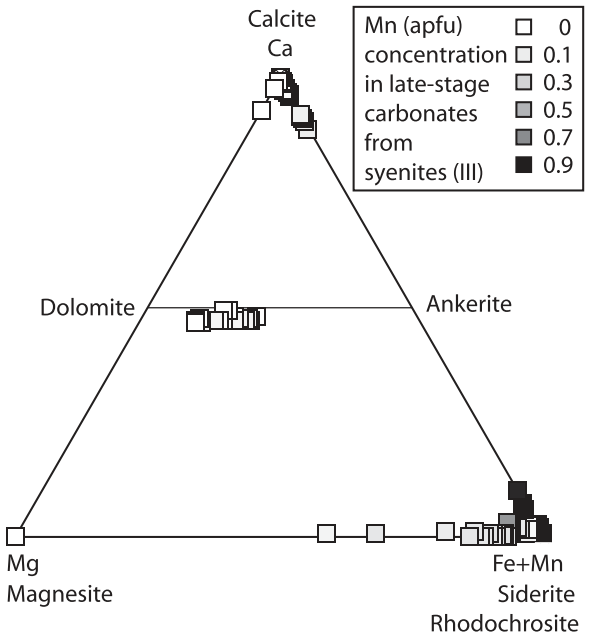

Fig. 9. Ternary plot showing compositions of carbonates from late-stage assemblages in syenites in the system Ca–Mg–(Fe + Mn). Grey scales allow for the distinction between Mn- and Fe-rich compositions.

Table 8: Representative compositions (wt %) of carbonate minerals from late-stage assemblages from syenites from Mont Saint-Hilaire

Sample:	VMA 2	T644	VMA 9	MOC3090	MOC3089
Analysis:	Carb 40	Carb 158	Carb 134	Carb 10	Carb 13
CaO	54·18	1·12	0·98	28·06	28·65
FeO	0·03	57·41	0·66	8·22	10·84
MnO	0·99	2·04	58·19	0·19	0·77
MgO	0·04	0·65	0·12	17·63	14·53
SrO	0·11	b.d.l.	b.d.l.	0·05	0·18
Na_2O	0·06	b.d.l.	0·26	0·11	b.d.l.
Al_2O_3	b.d.l.	b.d.l.	b.d.l.	0·01	0·08
TiO_2	b.d.l.	b.d.l.	0·01	b.d.l.	0·01
ZrO_2	b.d.l.	b.d.l.	b.d.l.	b.d.l.	0·03
Ce_2O_3	0·08	0·03	0·01	0·03	b.d.l.
Y_2O_3	0·08	0·06	b.d.l.	b.d.l.	0·05
SiO_2	0·02	b.d.l.	0·21	b.d.l.	b.d.l.
CO_2*	43·36	38·04	37·92	46·62	45·68
Total	98·94	99·35	98·36	100·92	100·81
Formulae based on 1 cation					
Ca	0·98	0·02	0·02	0·47	0·49
Fe	0·00	0·92	0·01	0·11	0·15
Mn	0·01	0·03	0·95	0·00	0·01
Mg	0·00	0·02	0·00	0·41	0·35
Sr	0·00	–	–	0·00	0·00
Na	0·00	–	0·01	0·00	–
Al	–	–	–	0·00	0·00
Ti	–	–	0·00	–	0·00
Zr	–	–	–	–	0·00
Ce	0·00	0·00	0·00	0·00	–
Y	0·00	0·00	–	–	0·00
Si	0·00	–	0·00	–	–
Mineral	Calcite	Siderite	Rhodochrosite	Dolomite	Dolomite

*CO_2 calculated assuming stoichiometry; b.d.l., below detection limit.

Age-corrected ε_{Nd} data for gabbros ($\varepsilon_{Nd} = 4{\cdot}8$) given by Foland *et al.* (1988) are analytically indistinguishable from our data and, combined with radiogenic isotope Sr data ($\varepsilon_{Sr} = -19$), have been interpreted to reflect derivation from an isotopically depleted mantle source and limited assimilation of crustal material (Foland *et al.*, 1988). Aegirine-rich clinopyroxene from two samples with hydrothermal textures gave lower ε_{Nd} values of 3·9 and 3·4, which indicates increasing degrees of assimilation in the late-stage evolution of the syenites (Fig. 11).

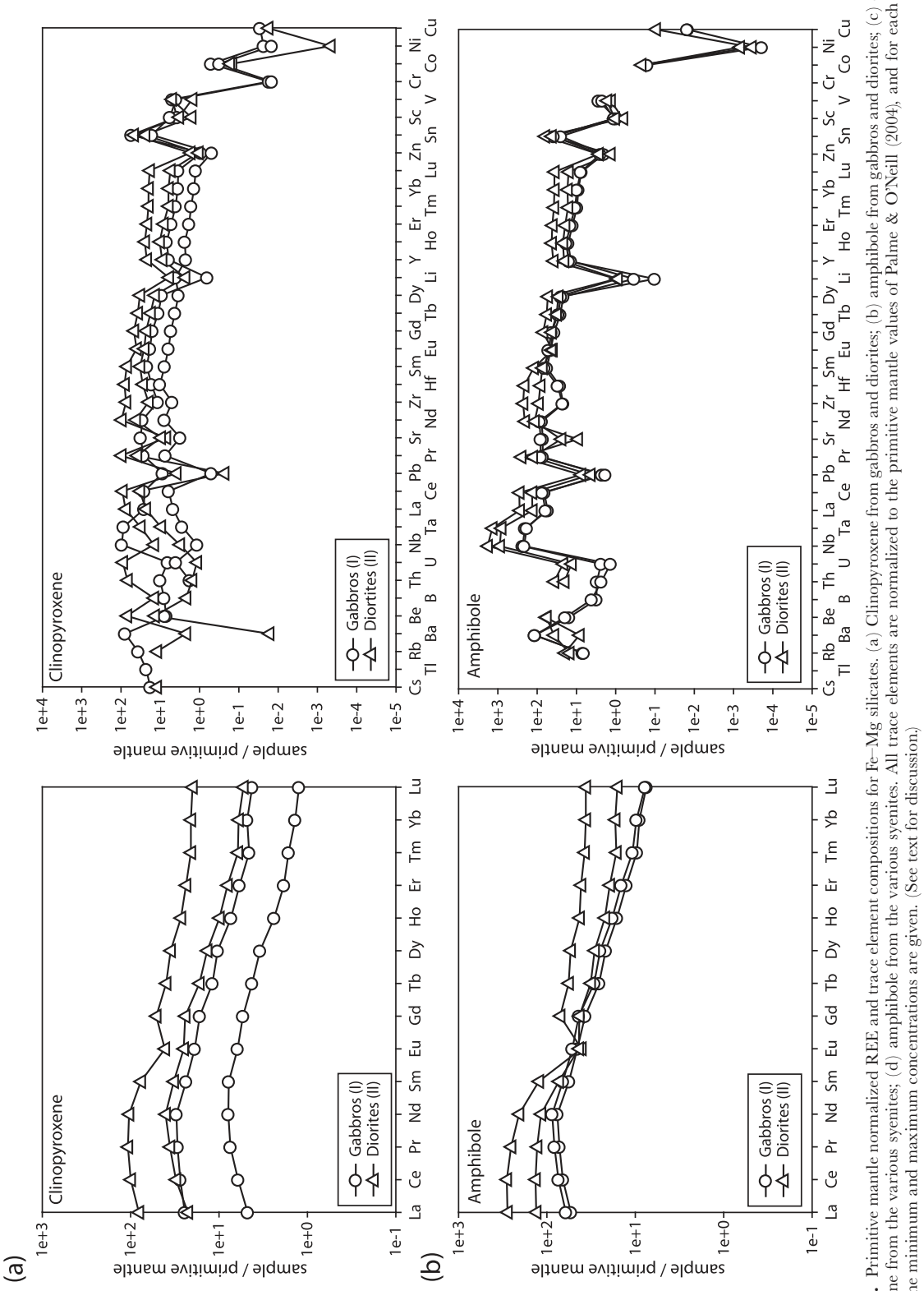

Fig. 10. Primitive mantle normalized REE and trace element compositions for Fe–Mg silicates. (a) Clinopyroxene from gabbros and diorites; (b) amphibole from gabbros and diorites; (c) clinopyroxene from the various syenites; (d) amphibole from the various syenites. All trace elements are normalized to the primitive mantle values of Palme & O'Neill (2004), and for each (sub-)unit the minimum and maximum concentrations are given. (See text for discussion.)

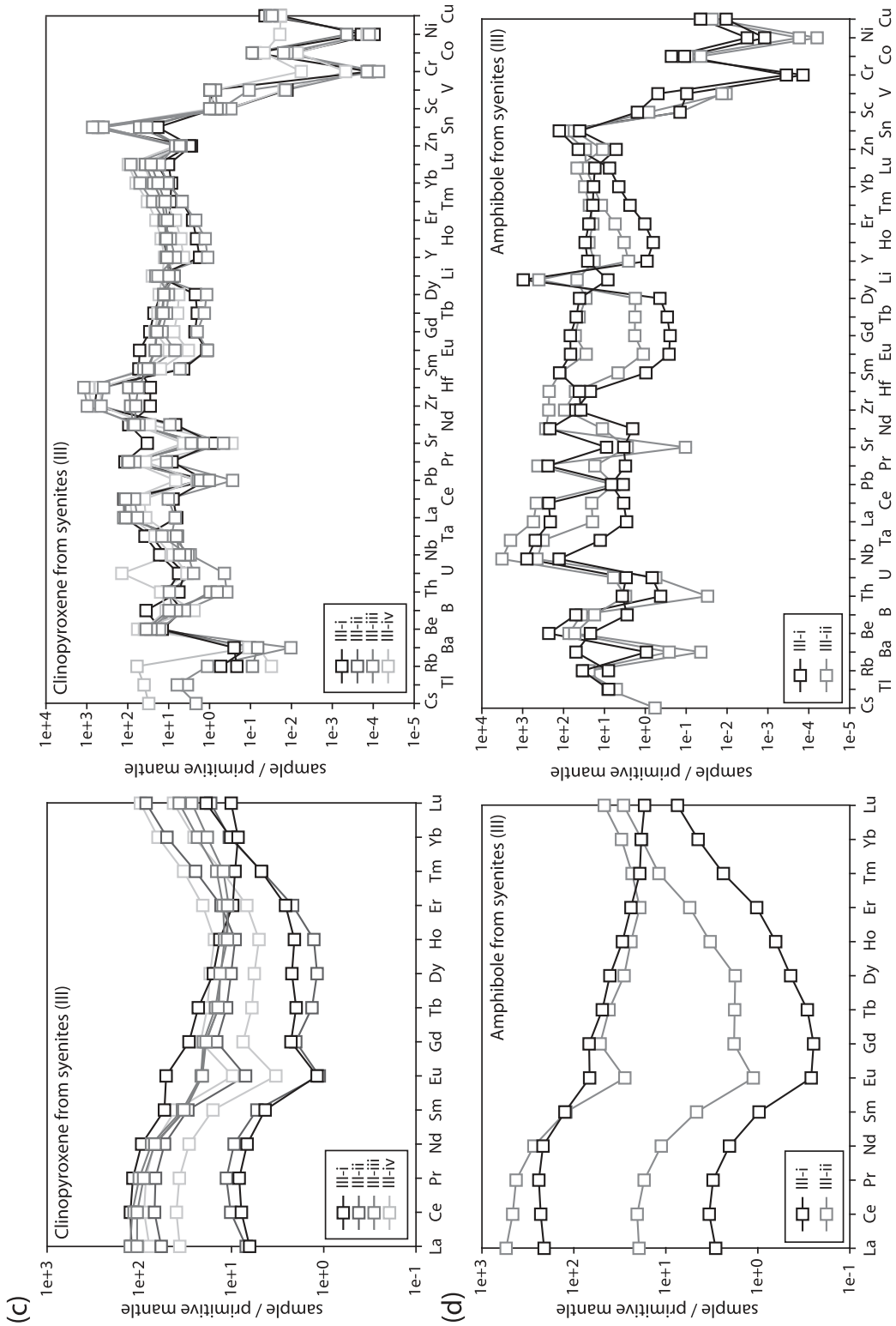

Fig. 10. Continued.

Table 9: Representative trace element compositions (ppm) of clinopyroxene (Cpx) and amphibole (Amp) from Mont Saint-Hilaire

Sample:	MSH 116 (I)	MSH 116 (I)	MSH 119 (II)	MSH 12 (II)	MSH 25 (III-i)	MSH 54 (III-ii)	MSH 105 (III-iii)	MSH 51 (III-iv)	MSH 17 (I)	MSH 75 (II)	MSH 25 (III-i)	MSH 54 (III-ii)
Analysis:	Cpx 6	Cpx 1	Cpx 4	Cpx 2	Cpx 3	Cpx 4	Cpx 7	Cpx 2	Amp 2	Amp 1	Amp 1	Amp 2
Li	5·10	1·03	3·73	10·2	9·64	29·4	15·7	37·7	0·55	0·94	3·86	452
Be	b.d.l.	0·49	0·97	3·39	0·54	2·03	2·47	2·03	1·07	1·14	0·55	4·90
B	b.d.l.	2·07	0·57	3·29	8·13	2·11	2·54	1·92	0·80	b.d.l.	0·60	8·72
P	53·2	257	97·5	80·5	44·0	15·5	31·6	12·8	251	155	113	2·86
Sc	97·3	61·5	26·8	51·0	8·48	8·81	16·4	6·28	16·2	18·8	10·1	7·29
V	336	427	440	130	180	9·30	84·1	1·22	236	149	149	4·42
Cr	97·1	43·4	b.d.l.	b.d.l.	1·19	0·19	b.d.l.	b.d.l.	b.d.l.	b.d.l.	1·82	0·19
Co	31·6	52·0	17·3	14·7	12·6	1·59	9·28	0·64	18·8	21·4	18·2	8·88
Ni	25·5	43·4	b.d.l.	1·30	0·83	0·23	b.d.l.	b.d.l.	b.d.l.	0·69	1·14	0·27
Cu	b.d.l.	0·58	b.d.l.	b.d.l.	0·49	0·59	b.d.l.	0·37	0·30	b.d.l.	0·41	0·92
Zn	27·3	49·2	57·3	92·8	66·3	266	284	304	108	96·5	110	1210
Rb	b.d.l.	22·1	b.d.l.	4·83	b.d.l.	0·68	b.d.l.	2·71	4·21	5·33	2·38	17·7
Sr	64·0	645	197	84·5	1109	57·0	30·9	1·07	1461	866	2529	121
Y	9·71	26·7	39·1	97·5	39·5	30·2	47·9	37·2	60·9	135	43·9	16·2
Zr	54·3	126	217	778	84·5	10536	688	5930	235	775	73·5	6968
Nb	0·95	56·1	1·88	9·13	5·24	1·97	3·20	13·3	139	681	81·1	333
Sn	2·42	7·54	3·36	6·37	1·33	99·4	4·75	43·6	3·45	6·47	4·42	48·2
Cs	b.d.l.	0·32	b.d.l.	0·22	b.d.l.	0·04	b.d.l.	0·1	b.d.l.	b.d.l.	b.d.l.	b.d.l.
Ba	b.d.l.	533	0·11	4·11	0·14	0·07	b.d.l.	b.d.l.	773	1383	1483	3·20
La	4·02	17·6	16·1	55·3	28·9	39·7	77·0	60·6	36·8	107	37·5	36·0
Ce	12·4	46·1	58·9	178	105	122	203	164	118	321	116	86·4
Pr	1·98	7·24	10·6	29·0	17·8	18·0	25·1	22·1	19·4	50·0	18·8	10·4
Nd	10·9	37·9	56·2	139	87·2	70·6	89·9	80·3	101	233	97·0	31·6
Sm	3·07	9·48	14·2	33·1	19·9	12·8	13·7	13·7	24·3	51·8	21·5	4·11
Eu	1·07	2·98	4·15	6·64	7·96	1·14	3·45	1·15	7·34	11·9	7·46	0·38
Gd	2·91	9·17	13·1	29·3	16·1	8·27	11·0	8·38	21·1	41·5	17·9	2·11
Tb	0·40	1·18	1·86	4·16	2·20	1·19	1·45	1·26	2·70	5·62	2·16	0·32
Dy	2·43	6·53	9·89	25·1	9·92	7·19	9·39	7·85	15·4	32·8	12·1	2·12
Ho	0·42	1·10	1·65	4·29	1·82	1·45	1·81	1·62	2·57	5·70	1·94	0·74
Er	0·89	2·45	3·86	11·0	3·40	6·04	4·99	7·01	5·88	13·8	4·19	3·43
Tm	0·12	0·29	0·44	1·49	0·41	1·76	0·88	1·97	0·69	1·79	0·49	1·12
Yb	0·61	1·65	2·85	9·61	2·02	23·1	8·44	25·1	4·15	10·4	2·68	11·6
Lu	0·10	0·25	0·40	1·42	0·30	5·98	1·91	6·52	0·53	1·42	0·33	2·72
Hf	3·11	5·03	8·43	24·5	2·16	354	16·8	178	7·93	20·8	1·89	222
Ta	0·12	3·46	0·39	1·30	1·04	0·58	0·26	1·75	8·14	33·4	3·71	18·2
Tl	b.d.l.	0·07	b.d.l.	b.d.l.	b.d.l.	0·02	b.d.l.	b.d.l.	b.d.l.	b.d.l.	b.d.l.	0·02
Pb	b.d.l.	1·61	0·04	0·52	0·04	0·35	0·19	1·58	0·42	0·66	0·67	1·20
Th	0·27	0·84	0·13	3·93	0·14	0·80	0·05	0·76	0·25	1·05	0·18	0·03
U	0·07	0·14	0·03	0·84	0·02	0·05	b.d.l.	0·68	0·05	0·15	0·04	0·04

b.d.l., below detection limit. Major element compositions are given in Tables 3 (clinopyroxene) and 4 (amphibole).

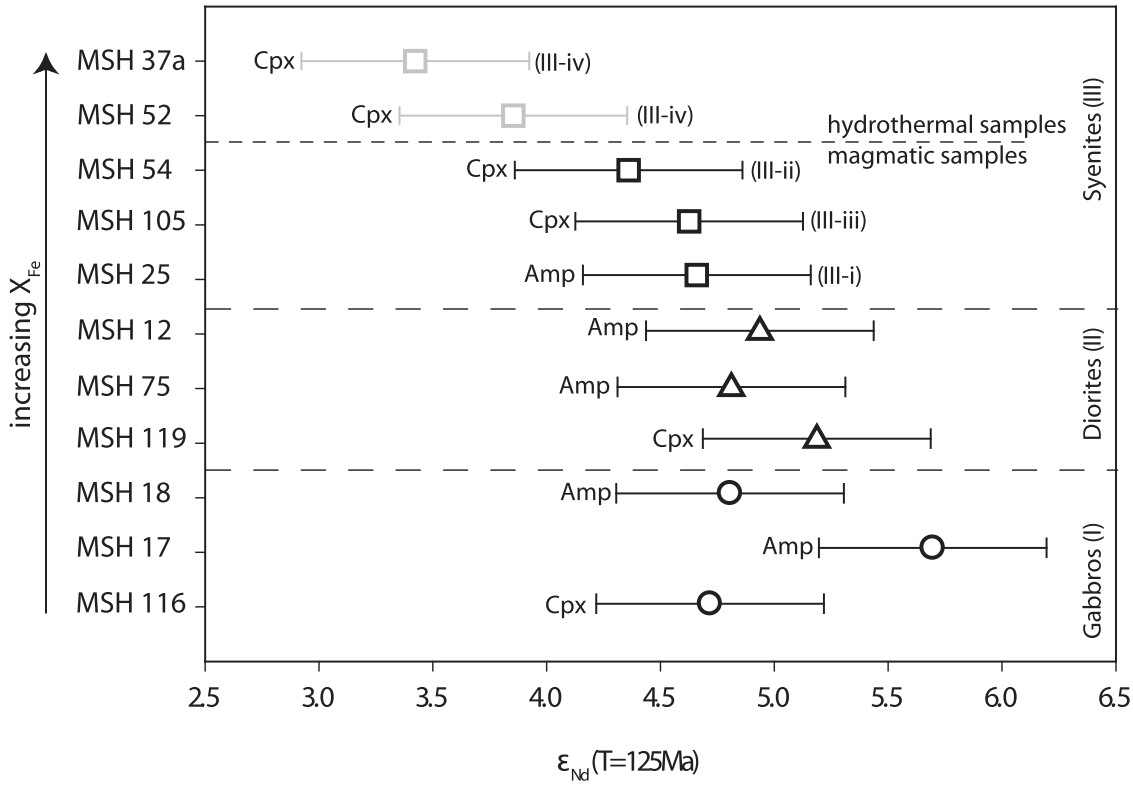

Fig. 11. Age-corrected ε_{Nd} data for representative samples from all units, sorted according to increasing X_{Fe} of the mineral separate analyzed. Clinopyroxene from samples MSH 52 and 37a display hydrothermal textures.

Stable isotopes

Oxygen in silicates

Forty-two hand-picked mineral separates of clinopyroxene, amphibole, biotite, olivine, feldspar and quartz from 30 representative samples were analyzed for their oxygen isotopic composition (Fig. 12, Table 10). Biotite, clinopyroxene and amphibole from gabbros vary in the range $\delta^{18}O = 3{\cdot}9$–$5{\cdot}1$‰; Fe–Mg silicates from diorites and syenites have $\delta^{18}O = 4{\cdot}8$–$5{\cdot}7$‰ and 4·2–6·3‰, respectively. Δcpx–amp values for clinopyroxene (cpx) and amphibole (amp) in apparent textural equilibrium are positive and range from 0·2 to 0·4‰ in gabbros and diorites and from 0·6 to 1‰ in syenites. Δcpx–ol is either positive (0·2) or negative (−0·1) in diorites and Δcpx–bt is negative (−0·4 to −0·7) in gabbroic and dioritic samples, whereas in syenites Δcpx–bt is positive (0·3–0·7).

Clinopyroxene from the late-stage assemblages of the syenites is isotopically indistinguishable from clinopyroxene with magmatic textures ($\delta^{18}O = 5{\cdot}1$–6‰). Albite and orthoclase from late-stage assemblages have $\delta^{18}O = 10{\cdot}1$ and 14·2‰ respectively, and late-stage quartz exhibits the highest value of $\delta^{18}O = 18{\cdot}9$‰.

Hydrogen in silicates

δD values for amphibole and biotite from gabbros and diorites vary in a narrow range between −64 and −95‰. In the syenites, amphibole and biotite vary between δD = −107 and −156‰, with the lowest δD values for those samples with highest X_{Fe}. All mineral separates plot below the meteoric water line (Fig. 13, Table 10) and have similar hydrogen isotopic compositions to hydrosilicates from other alkaline occurrences (Marks *et al.*, 2004*b*; Waczek, 2009), although our data extend to higher values with respect to the hydrosilicates from Mont Saint-Hilaire reported by Waczek (2009).

Oxygen and carbon in carbonates

Post-magmatic siderite, rhodochrosite and magnesite from late-stage samples in the syenites yield $\delta^{18}O$ and $\delta^{13}C$ values between 9·2 and 18·9‰ and between −5·3 and 2·2‰, respectively (Fig. 14, Table 10). Dolomite-group minerals are characterized by $\delta^{18}O$ and $\delta^{13}C$ values of 12–13·3‰ and −2·5 to −1·2‰, respectively. Texturally latest calcite has $\delta^{18}O$ values of 12–26·3‰ and $\delta^{13}C$ values of −5·2 to 2·3‰. Data for coarse-grained

Table 10: Isotopic compositions of mineral separates from Mont Saint-Hilaire

Sample	Unit	ε_{Nd} (T = 125 Ma) (mineral)	$\delta^{18}O_{VSMOW}$ (‰) (mineral)	δD_{VSMOW} (‰) (mineral)	$\delta^{13}C_{PDB}$ (‰) (mineral)
MSH 116	I	4·7 (Cpx)	5·1 (Cpx)		
			4·9 (Amp)	−116 (Amp)	
MSH 17	I	5·7 (Amp)	4·2 (Amp)	−84 (Amp)	
			4·6 (Cpx)		
MSH 18	I	4·8 (Amp)	3·9 (Amp)	−86 (Amp)	
			4·1 (Cpx)		
			4·8 (Bt)	−87 (Bt)	
MSH 119	II	5·2 (Cpx)	5·0 (Cpx)		
			4·8 (Ol)		
			5·1 (Bt)	−81 (Bt)	
MSH 75	II	4·8 (Amp)	5·2 (Amp)	−75 (Amp)	
			5·6 (Bt)	−82 (Bt)	
MSH 12	II	4·9 (Amp)	5·1 (Amp)	−81 (Amp)	
			5·3 (Cpx)		
			5·4 (Ol)		
			5·7 (Bt)	−64 (Bt)	
MSH 25	III-i	4·7 (Amp)	5·2 (Amp)	−107 (Amp)	
			4·2 (Cpx)		
MSH 105	III-iii	4·6 (Cpx)	5·0 (Cpx)		
			4·3 (Bt)	−112 (Bt)	
MSH 54	III-ii	4·4 (Cpx)	5·8 (Cpx)		
			5·2 (Amp)	−156 (Amp)	
			5·5 (Bt)	−115 (Bt)	
MSH 52	III-iv	3·9 (Cpx)	5·4 (Cpx)		
MSH 37a	III-iv	3·4 (Cpx)	5·3 (Cpx)		
MSH 37b	III-i		5·4 (Cpx)		
MSH 29a	III-iv		6·3 (Cpx)		
MSH 29b	III-iv		5·7 (Cpx)		
MSH 59	III-iv		5·3 (Cpx)		
MSH 68	III-iv		5·3 (Cpx)		
MSH 51	III-iv		5·0 (Cpx)		
MSH 40	III-iii		5·1 (Cpx)		
MSH 50	III-ii		5·5 (Cpx)		
MSH 148	late-stage in III		5·1 (Cpx)		
MOC 396	late-stage in III		6·0 (Cpx)		
	late-stage in III		11·6 (Ab)		
MOC 266	late-stage in III		10·1 (Ab)		
49692	late-stage in III		11·0 (Ab)		
48801	late-stage in III		12·1 (Ab)		
48751	late-stage in III		12·2 (Ab)		

(continued)

Table 10: Continued

Sample	Unit	ε_{Nd} (T = 125 Ma) (mineral)	$\delta^{18}O_{VSMOW}$ (‰) (mineral)	δD_{VSMOW} (‰) (mineral)	$\delta^{13}C_{PDB}$ (‰) (mineral)
MSH 34	late-stage in III		14·2 (Or)		
MOC 1485	late-stage in III		18·9 (Qz)		
MSH 34	late-stage in III		21·6 (Cal)		−3·9 (Cal)
			14·3 (Rds)		−3·0 (Rds)
MSH 66	marble xenolite		26·3 (Cal)		2·3 (Cal)
LH 1	late-stage in III		10·8 (Sabinaite)		−3·7 (Sabinaite)
LH 2	late-stage in III		14·9 (Cal)		−0·4 (Cal)
LH 3	late-stage in III		10·3 (Synchysite)		−2·8 (Synchysite)
LH 4	late-stage in III		17·8 (Dawsonite)		−2·2 (Dawsonite)
LH 5	late-stage in III		20·8 (Ancyllite)		−0·7 (Ancyllite)
LH 6	late-stage in III		19·0 (Cal)		−1·9 (Cal)
LH 7	late-stage in III		13·3 (Dol)		−1·2 (Dol)
LH 8	late-stage in III		13·4 (Dawsonite)		−2·9 (Dawsonite)
LH 9	late-stage in III		12·5 (Rds)		−3·3 (Rds)
LH 10	late-stage in III		14·1 (Shortite)		2·2 (Shortite)
LH 11	late-stage in III		10·3 (Sd)		−4·3 (Sid)
MOC 3090	late-stage in III		12·9 (Dol-I)		−2·1 (Dol-I)
	late-stage in III		12·8 (Dol-II)		−1·4 (Dol-II)
MOC 3089	late-stage in III		12·0 (Dol-I)		−2·5 (Dol-I)
	late-stage in III		12·3 (Dol-II)		−1·8 (Dol-II)
T 308	late-stage in III		13·3 (Cal)		−3·4 (Cal)
	late-stage in III		18·4 (Sd)		2·2 (Sd)
	late-stage in III		18·9 (Mgs)		1·9 (Mgs)
49692	late-stage in III		21·8 (Cal)		−5·2 (Cal)
T 650	late-stage in III		19·1 (Cal)		−3·8 (Cal)
	late-stage in III		9·2 (Sd)		−5·2 (Sd)
49049	late-stage in III		12·4 (Cal)		−1·4 (Cal)
	late-stage in III		10·4 (Sd)		−3·7 (Sd)
	late-stage in III		10·4 (Dol)		−2·7 (Dol)
48751	late-stage in III		20·7 (Cal)		−2·9 (Cal)
	late-stage in III		9·9 (Sd)		−4·6 (Sd)
48801	late-stage in III		20·0 (Cal)		−2·7 (Cal)
	late-stage in III		10·5 (Sd)		−4·5 (Sd)
MOC 266	late-stage in III		12·0 (Cal)		−2·2 (Cal)
MOC 393	late-stage in III		24·6 (Cal)		1·6 (Cal)
MOC 396	late-stage in III		18·0 (Cal)		−3·0 (Cal)
MOC 1485	late-stage in III		18·7 (Cal)		−1·3 (Cal)

Dol-I and Dol-II refer to different dolomite generations found in the same sample.

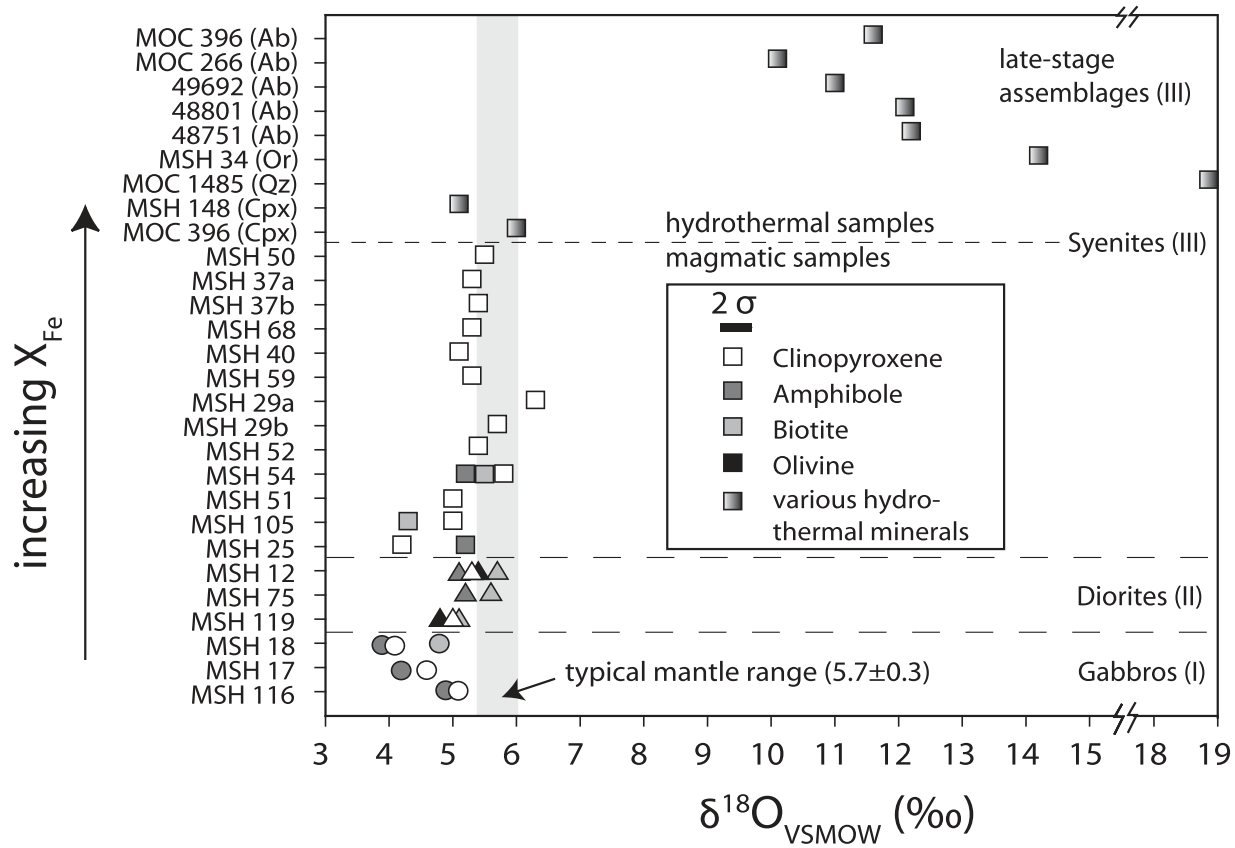

Fig. 12. $\delta^{18}O_{VSMOW}$ (‰) data for mineral separates from all units. Fe–Mg silicates are sorted according to increasing X_{Fe}. Different grey scales represent different minerals; gabbros are represented by circles, diorites by triangles and syenites by squares.

calcite from a marble xenolith and calcite from one late-stage mineral association overlap with the oxygen and carbon isotope compositions of the St. Lawrence Lowland limestones (Carignan *et al.*, 1997). Other carbonate minerals range from 10 to 21‰ ($\delta^{18}O$) and −4 to 2‰ ($\delta^{13}C$).

Fluid inclusions

Fluid inclusions from the various Mont Saint-Hilaire lithologies are interpreted to be of secondary origin. Two groups of fluid inclusions can be recognized based on composition (Figs 15 and 16, Table 11), as follows.

Group (a) fluid inclusions are CO_2-dominated two-phase (V + L) fluid inclusions with volume fractions φ between 0·6 and 0·95 at room temperature. Group (a) fluid inclusions are entrapped in variably sized secondary trails in all minerals of the gabbros and diorites and in some late-stage minerals of the syenites (Figs. 15a and d) and are commonly <20 μm in size and regular to irregular in shape (e.g. in apatite, nepheline and cryolite). Final melting occurs between −60·7 and −56·6°C (Fig. 16a) and slight depressions of the triple point of CO_2 result from the presence of minor amounts of CH_4 detected by Raman spectroscopy; further species present in group (a) fluid inclusions include HSO_4^-, SO_2 and H_2O. Temperatures of CO_2 homogenization range from 22 to 30°C and homogenization into the liquid is observed for all samples except for a late-stage cryolite (Fig. 16a, Table 11). Based on low degrees of fill we assume total homogenization, which was not observed owing to low concentrations of H_2O in carbonic fluid inclusions, to have occurred in the course of a dew point transition.

Group (b) fluid inclusions are two-phase (V + L) aqueous fluid inclusions at room temperature with variable salinities, which are characterized by volume fractions φ between 0·75 and 0·99 (Fig. 15b–d). Secondary aqueous group (b) fluid inclusions are mostly irregular in shape, variable in size (but mostly <100 μm) and occur as isolated individuals or are arranged in trails. In some late-stage

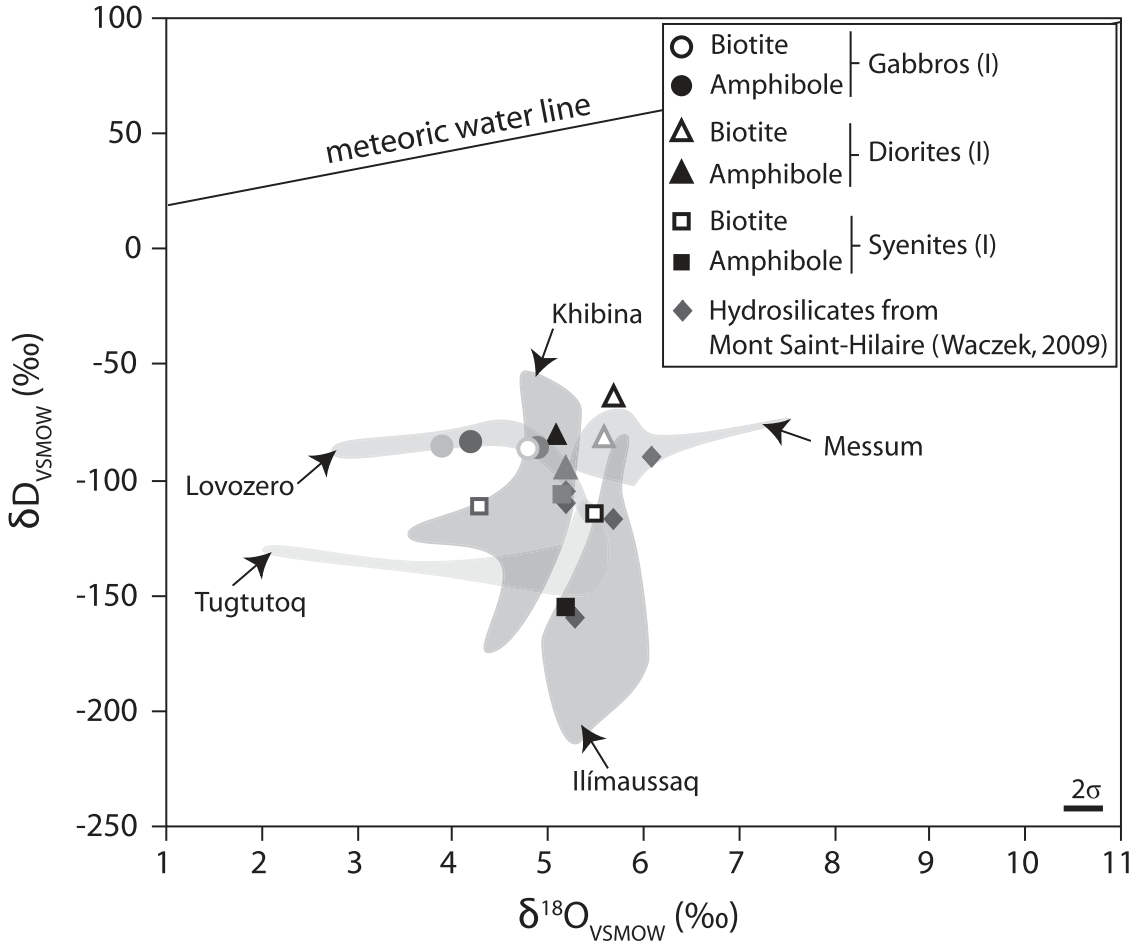

Fig. 13. $\delta^{18}O_{VSMOW}$ (‰) vs δD_{VSMOW} (‰) of hydrosilicates. Open symbols represent biotite; closed symbols stand for amphibole. Grey scales are identical for minerals from the same sample. The O and H isotope compositions of hydrosilicates from Mont Saint-Hilaire are from Waczek (2009) and are shown as diamonds (Mont Saint-Hilaire) and grey fields (other alkaline rock occurrences).

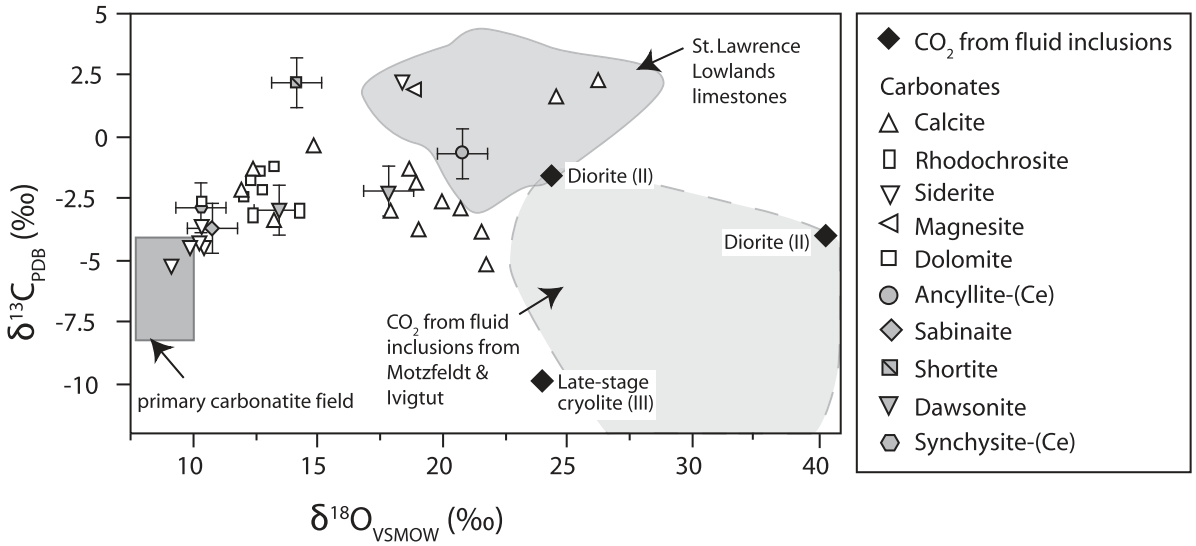

Fig. 14. $\delta^{18}O_{VSMOW}$ CO_2 (‰) vs $\delta^{13}C_{PDB}$ CO_2 (‰) for carbonates and CO_2 extracted from fluid inclusions. The primary carbonatite field is from Taylor *et al.* (1967), the limestone field is from Carignan *et al.* (1997) and the CO_2 of fluid inclusions is from Köhler *et al.* (2008; Ivigtut) and Schönenberger & Markl (2008; Motzfeldt).

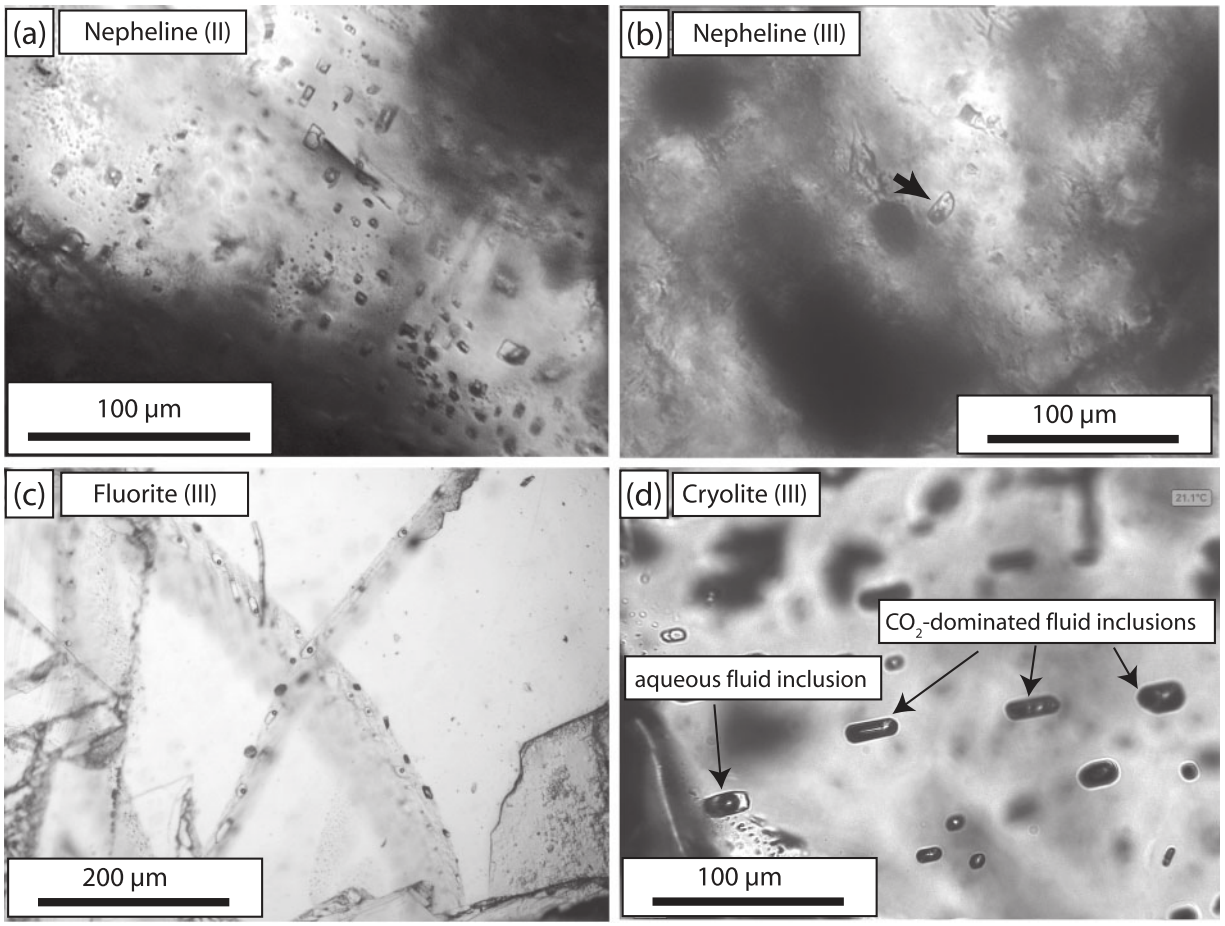

Fig. 15. Photomicrographs of fluid inclusions. (a) Variably sized secondary group (a) CO_2-rich fluid inclusions in nepheline from diorite; (b) irregularly shaped secondary group (b) aqueous fluid inclusion in nepheline from a syenitic sample; (c) intersecting trails (healed fractures?) of group (b) aqueous fluid inclusions found in a late-stage fluorite in syenites; (d) trail of secondary fluid inclusions consisting of cogenetic CO_2-dominated [group (a)] and aqueous [group (b)] fluid inclusions in a late-stage cryolite found in a syenite; the identical orientation of carbonic and aqueous fluid inclusions and different volume fractions φ should be noted.

samples (e.g. a fluorite), aqueous fluid inclusions found in trails yield similar total homogenization and final melting temperatures (Fig. 16b) and thus are interpreted to be cogenetic and not to have been modified under post-entrapment conditions. For most (magmatic) samples, strongly differing total homogenization and final melting temperatures of aqueous fluid inclusions may result from mixing of internal fluids with variable proportions of external fluids (sample MSH 54, Fig. 16b). Clathrate melting was observed only in some fluid inclusions (e.g. in a fluorite, clathrate disappeared at temperatures of 9–13°C) but often, was not reproducible owing to metastable behavior. Volatile species detected by Raman spectroscopy in aqueous fluid inclusions include SO_4^{2-}, HSO_4^-, SO_2 and either CO_2 or CH_4. Salinities range from 1 to 25·6 wt % NaCl equivalent (calculated after Bodnar, 1993) and the observation of final melting temperatures below −20·8°C argues for the presence of salts such as $CaCl_2$ in addition to NaCl. In rare samples of all units, aqueous group (b) fluid inclusions were found to form individuals in up to millimeter-sized trails that are dominated by carbonic group (a) fluid inclusions (Fig. 15d), which indicates heterogeneous trapping from an immiscibly coexisting aqueous–carbonic fluid that migrated through all rock units under sub-solidus conditions.

Three out of 10 samples yielded sufficient CO_2 during crushing to analyze the fluid inclusion-extracted CO_2 for its oxygen and carbon isotopic composition. Carbon dioxide from a dioritic sample and a late-stage cryolite yield indistinguishable $\delta^{18}O$ values of 24·4 and 24‰, respectively, and thus overlap with some late-stage carbonates and sedimentary limestone hosts with respect to their oxygen isotopic composition (Fig. 14). Carbon dioxide from CO_2 from another diorite has a higher $\delta^{18}O$ value of 40‰. $\delta^{13}C$ values for the three samples differ and were analyzed to be −2‰ and −4‰ for carbon from CO_2 from fluid

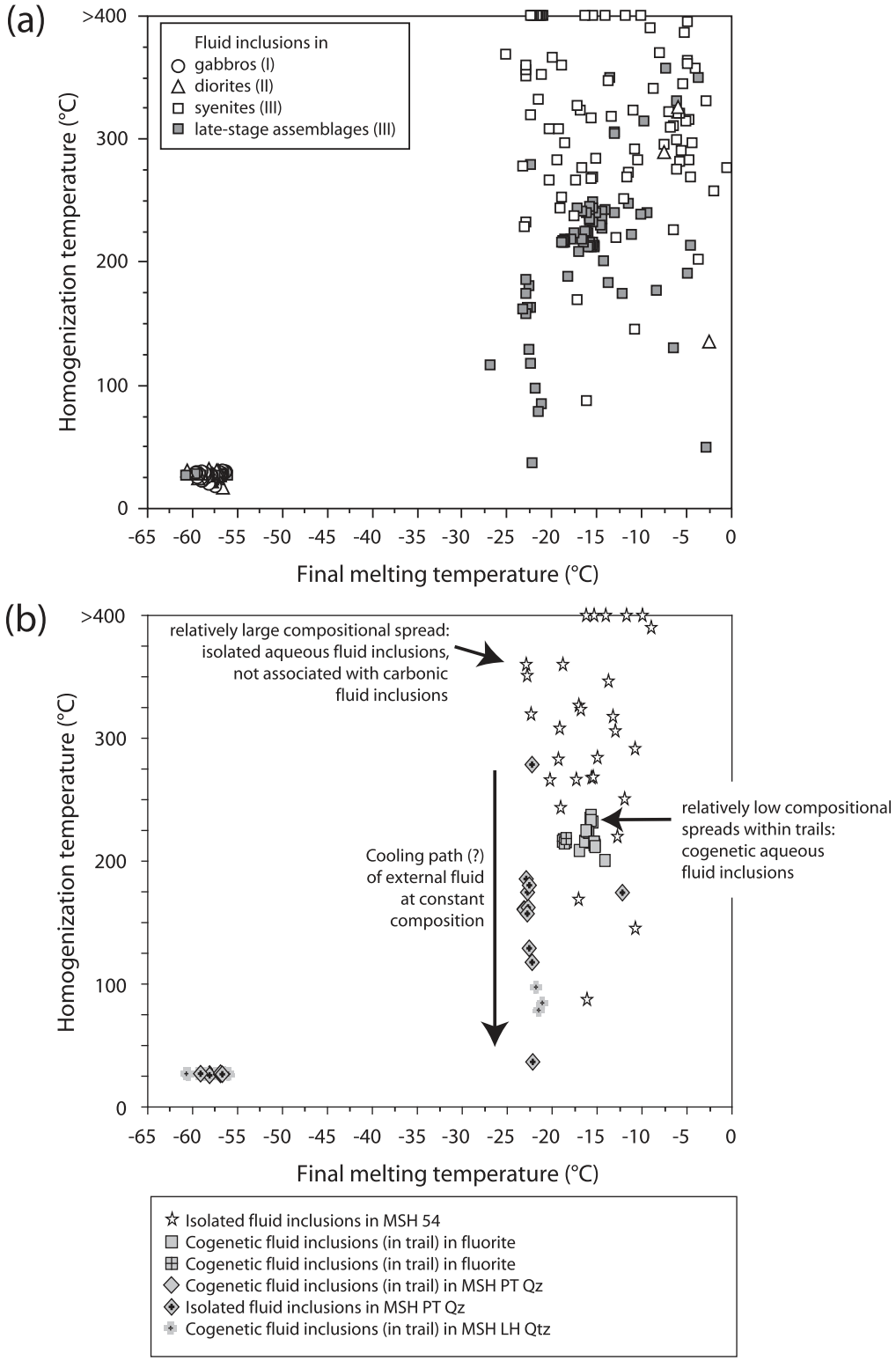

Fig. 16. Microthermometry results of fluid inclusion investigations. (a) Final melting temperature vs homogenization temperature of all fluid inclusions. (b) Assemblage approach for selected fluid inclusions from the syenites (magmatic and late-stage samples). The large compositional spread of aqueous fluid inclusions in sample MSH 54 that are not associated with carbonic fluid inclusions is interpreted to reflect capture of a magmatic fluid that became subsequently mixed with an external fluid.

Table 11: Characteristics of fluid inclusions from Mont Saint-Hilaire

Sample	Unit	Incl no.	Host mineral	Composition	Degree of fill	Phases	Homogenization type	*T* of final melting (°C)	Homogenization *T* (°C)	Salinity (wt % NaCl equiv.)
MSH 18	I	9	Plag	carbonic	0·85	v-l	>l	−56·3	29	n.a.
MSH 18	I	10	Plag	carbonic	0·8	v-l	>l	−56·8	26	n.a.
MSH 115	I	8	Ap	carbonic	0·7	v-l	>l	−59·2	28	n.a.
MSH 115	I	9	Ap	carbonic	0·9	v-l	>l	−58·9	30	n.a.
MSH 113	I	15	Ap	carbonic	0·5	v-l	>l?	−58·5	26	n.a.
MSH 113	I	16	Ap	carbonic	0·5	v-l	>l?	−58·5	27	n.a.
MSH 75	II	1	Nph	carbonic	0·8	v-l	>l	−56·8	28	n.a.
MSH 75	II	2	Nph	carbonic	0·8	v-l	>l	−56·8	26	n.a.
MSH 12	II	1	Nph	carbonic	0·65	v-l	>l	−58·0	23	n.a.
MSH 12	II	2	Nph	carbonic	0·75	v-l	>l	−57·7	24	n.a.
MSH 119	II	15	Ap	aqueous	0·99	v-l	>l	−2·5	135	4·2
MSH 119	II	10	Ap	carbonic	0·8	v-l	>l	−57·1	31	n.a.
MSH 25	III-i	1	Nph	aqueous	0·95	v-l	>l	−2·8	330	4·6
MSH 54	III-ii	12	Nph	aqueous	0·95	v-l	>l	−22·3	320	23·9
MSH 54	III-ii	13	Nph	aqueous	0·9	v-l	>l	−17·0	327	20·2
MSH 62	III-iv	12	Nph	aqueous	0·9	v-l	>l	−10·9	323	14·8
MSH 62	III-iv	13	Nph	aqueous	0·95	v-l	>l	−21·1	352	23·1
MSH 99	III-iii	14	Nph	aqueous	0·95	v-l	>l	−25·1	368	25·6
MSH 99	III-iii	1	Nph	aqueous	0·95	v-l	>l	−21·5	409	23·4
MSH 34	late stage in III	6	Cal	aqueous	0·95	v-l	>l	−18·1	188	21·0
MSH 34	late stage in III	7	Cal	aqueous	0·95	v-l	>l	−11·1	222	15·1
MSH__Fluorite__PT__2	late stage in III	1	Fluorite	aqueous	0·9	v-l	>l	−15·8	235	19·3
MSH__Fluorite__PT__3	late stage in III	2	Fluorite	aqueous	0·9	v-l	>l	−15·5	232	19·0
MSH__Quartz__PT__4	late stage in III	14	Qz	aqueous	0·95	v-l	>l	−22·9	186	24·3
MSH__Quartz__PT__5	late stage in III	15	Qz	carbonic	0·6	v-l	>l	−58·1	27	n.a.
MSH__Cryolite__PT__5	late stage in III	9	Cryolite	carbonic	0·7	v-l	>v	−57·0	25	n.a.
MSH__Cryolite__PT__5	late stage in III	10	Cryolite	carbonic	0·7	v-l	>v	−56·9	26	n.a.
MSH__Nepheline__PT__1	late stage in III	3	Nph	aqueous	0·95	v-l	>l	−6·0	299	9·2
MSH__Nepheline__PT__2	late stage in III	4	Nph	aqueous	0·9	v-l	>l	−6·4	310	9·7
T515	late stage in III	7	Anl	aqueous	0·95	v-l	>l	−7·2	357	10·8
T515	late stage in III	8	Anl	aqueous	0·95	v-l	>l	−4·5	213	7·1

All fluid inclusions are interpreted to be secondary in origin; n.a., not applicable. The full dataset is provided in the Electronic Appendix. v, vapour; l, liquid. Salinity values are calculated after Bodnar (1993).

inclusions in the diorites and −10‰ for carbon from CO_2 from the cryolite (Fig. 14).

DISCUSSION

The magmatic stage: intensive parameters

Field evidence suggests that the gabbros were emplaced first, followed by the diorites and syenites; this is in agreement with the conclusions of Greenwood & Edgar (1984) and the field evidence described by Rajasekaran (1967) and Currie (1989).

For the only olivine-bearing gabbro sample MSH 113, we followed the approach of Frost *et al.* (1988) and Schilling *et al.* (2011*a*) in calculating intensive parameters. Results from two-oxide oxythermometry, based on our analyzed compositions, define a linear trend in T–f_{O2} space and

cluster at 1100–1200°C. At 1100°C, the equilibrium between the Ca-Tschermak's component in clinopyroxene and anorthite (1) constrains a_{SiO2}:

$$CaAlAlSiO_6\,(Cpx) + SiO_2(liq) = CaAl_2Si_2O_8(Plag). \quad (1)$$

Applying the composition–activity formulation of McCarthy & Patiño Douce (1998), silica activities of ~0·5 are indicated based on core compositions. Using the most forsteritic olivine composition analyzed in sample MSH 113, we calculated the QUIlF surface in T–$\Delta\log f_{O2}$ (FMQ) space that titanomagnetite and ilmenite ideally would be in equilibrium with (Schilling *et al.*, 2011*a*). For the estimated $a_{SiO2} = 0{\cdot}5$, the calculated QUIlF surface intersects the linear trend based on T–$\Delta\log f_{O2}$ (FMQ) pairs from oxide thermometry and indicates equilibrium conditions of ~1190°C and $\log f_{O2} = 0{\cdot}7$ (ΔFMQ).

For the olivine-free gabbros, we calculated silica activity based on equilibrium (1) using core compositions of clinopyroxene and plagioclase at the highest temperature indicated by two-oxide oxythermometry for the respective samples at 1 kbar pressure (Currie *et al.*, 1986). To further constrain temperature and oxygen fugacity, we introduced the calculated silica activity and the respective clinopyroxene and Fe–Ti oxides compositions into the QUILF program (Andersen *et al.*, 1993) and allowed QUILF to vary the Mg-components in ilmenite, titanomagnetite and clinopyroxene to equilibrium values. If QUILF varied the Mg-component of clinopyroxene by more than 10 mol % to achieve equilibrium conditions, we used the analyzed (unchanged) clinopyroxene composition instead. For samples in which strongly secondary zoned crystals of plagioclase were found, we allowed QUILF to adjust the silica activity; in these cases, secondary processes are believed to have modified the original magmatic plagioclase compositions, which are interpreted to be out of equilibrium with the other co-magmatic minerals. Most olivine-free gabbros yield estimated temperatures of ~1100 to 735°C, a range of f_{O2} of −0·4 to +0·7 (ΔFMQ) and variable silica activities between 0·3 and 0·7. One gabbro sample gave an f_{O2} estimate of +1·9 (ΔFMQ) and we interpret this sample to have been compositionally modified under late-stage rather than magmatic conditions. Our results yield higher temperatures and lower oxygen fugacities than the estimates of Greenwood & Edgar (1984) and Currie *et al.* (1986). However, those workers stated that their results probably reflect subsolidus rather than primary magmatic conditions. Figure 17a summarises log f_{O2} and T estimates for the gabbros and diorites (Schilling *et al.*, 2011*a*) and shows that the gabbros crystallized under higher f_{O2} conditions than the diorites. Thus, our data and those presented by Schilling *et al.* (2011*a*) confirm the interpretation of Currie *et al.* (1986), who stated that the diorites crystallized under more reducing conditions than the gabbros. In terms of calculated silica activity–temperature equilibrium conditions, the gabbros and diorites are indistinguishable, although the diorites record lower variation between the samples investigated.

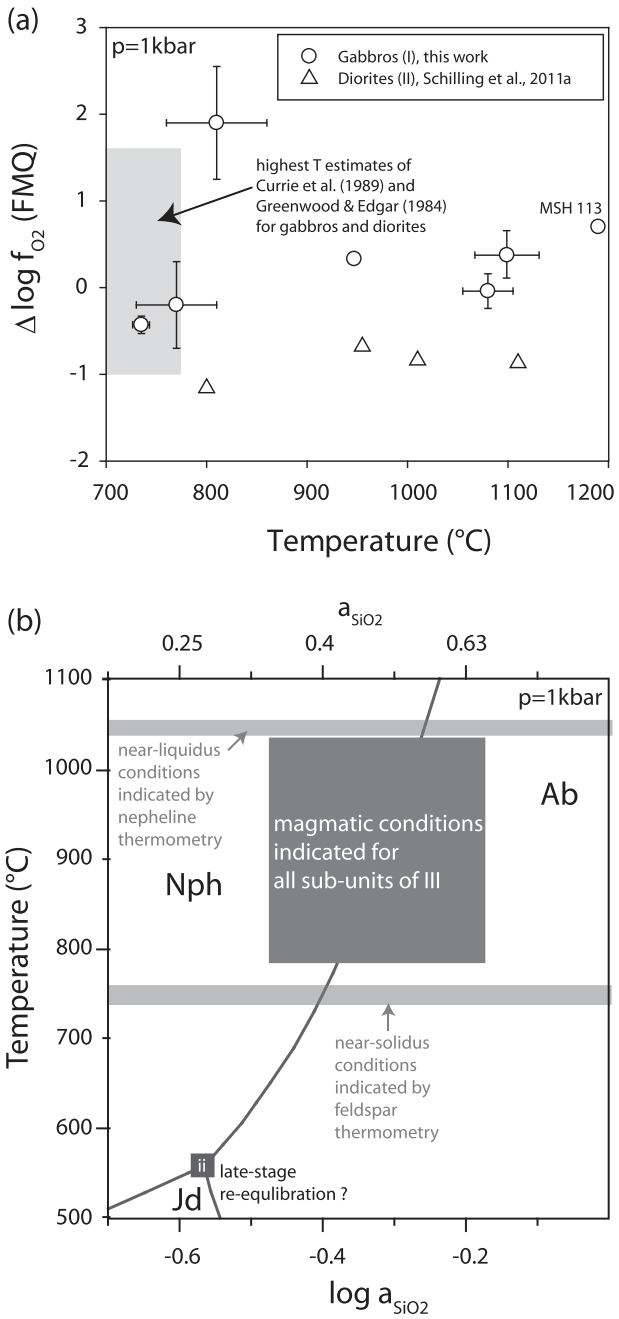

Fig. 17. (a) Temperature vs log f_{O2} plot for gabbros and diorites. Error bars account for uncertainties from the QUILF runs [see Schilling *et al.* (2011*a*) for discussion of the data from the diorites]. (b) Silica activity vs temperature based on equilibria (2)–(4) for the various foid syenites. Primary zonation patterns considered for T–a_{SiO2} estimates indicate conditions represented by the grey-shaded field for all sub-units of the foid syenites. Mineral compositions from one sample from III-ii indicate late-stage re-equilibration.

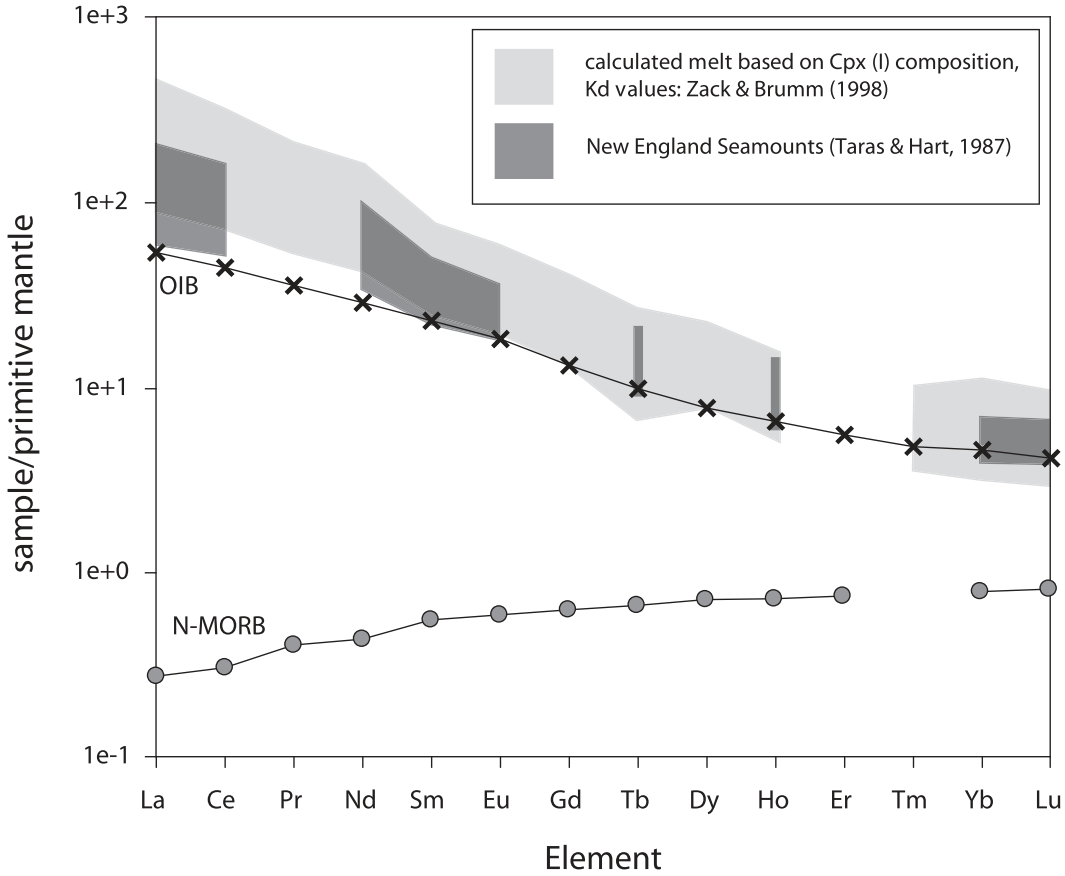

Fig. 18. Calculated melt composition (light grey) based on the analyzed REE concentrations in clinopyroxene from the most primitive gabbro, using the K_D values of Zack & Brumm (1998). Typical REE patterns for an OIB (crosses; Sun & McDonough, 1989), and a mid-ocean ridge basalt (MORB; circles; Workman & Hart, 2005) and trace element compositions of the New England Seamounts (dark grey; Taras & Hart, 1987) are shown for comparison.

The mineral assemblages of the various syenites do not allow oxygen fugacity to be constrained but equilibria between nepheline, alkali feldspar and clinopyroxene can be used to estimate temperature and silica activity (e.g. Mitchell & Platt, 1978; Markl *et al.*, 2001):

$$NaAlSiO_4\ (Nph) + SiO_2\ (liq) = NaAlSi_2O_6\ (Cpx) \quad (2)$$

$$NaAlSi_2O_6\ (Cpx) + SiO_2\ (liq) = NaAlSi_3O_8\ (Afs) \quad (3)$$

$$NaAlSiO_4\ (Nph) + 2SiO_2\ (liq) = NaAlSi_3O_8\ (Afs). \quad (4)$$

Endmember activities were calculated using an one-site mixing model for nepheline and applying the solution–activity formulation of Holland & Powell (2003) for clinopyroxene and feldspar. Figure 17b was calculated using the GEOCALC software of Berman *et al.* (1987) and Liebermann & Petrakakis (1990) with the database of Berman (1988). In the various syenites, a_{SiO2} varies between 0·65 and 0·3 and temperature estimates yield a range from >1000°C to 550°C based on the core compositions of nepheline, rare primary zoned clinopyroxene and reintegrated feldspar compositions (Fig. 17b). The highest temperatures derived from equilibria (2)–(4) are in agreement with the highest temperature estimates based on nepheline thermometry after Hamilton (1961; Fig. 8). If secondarily zoned clinopyroxene is considered, the whole range of T–a_{SiO2} conditions observed within unit III can be reconstructed from a single sample and hence, such samples must reflect disequilibrium conditions (Fig. 17b).

Constraining the source of the Mont Saint-Hilaire melt(s)

Trace elements

The trace element patterns of clinopyroxene and amphibole suggest a cogenetic relationship for all lithologies from gabbro to diorite. Increasing concentrations of the REE in clinopyroxene and amphibole are accompanied by the formation of a negative Eu anomaly (Fig. 10a and b). The first effect can be explained by the fractionation of

Fe–Ti oxides and plagioclase from the parental magma, which is evident from the petrography. Partition coefficients for REE in both Fe–Ti oxides and plagioclase are <1 (except for Eu in plagioclase; see below) in basaltic systems and hence, the REE are passively enriched during progessive crystallization (e.g. Lemarchand *et al.*, 1987; Bindeman & Davis, 2000). We attribute the formation of a negative Eu anomaly to the fractionation of plagioclase and, to a lesser degree, apatite. Partition coefficients for Eu have been reported by Villemant *et al.* (1981) for basaltic systems to exceed unity in plagioclase, but at least are higher for Eu than for the other REE. For apatite, Paster *et al.* (1974) found partition coefficients for Eu in basaltic systems to be greater than for the other REE and thus apatite is likely to deplete the magma in Eu and to co-contribute to the negative Eu anomalies found in the later crystallized minerals of the more evolved units.

The interpretation of the REE variation in the various syenites is more problematic, as the chemistry of both the melt and the Fe–Mg silicates differs fundamentally, with respect to major elements, compared with the gabbros and diorites. The following observations nevertheless are in favor of fractionation of the syenite magmas from more primitive mafic parents (gabbro and diorite). First, the REE patterns of clinopyroxene and amphibole from the fine-grained foid syenites (III-i) resemble those of clinopyroxene and amphibole in the diorites in terms of both concentration level and LREE–HREE distribution (Fig. 10c and d). Second, the more sodic rims of both clinopyroxene and amphibole overgrowing more calcic core compositions in some samples from the fine- and medium-grained foid syenites (III-I and -iii) invariably have a different REE distribution pattern. Thus, the major element composition of clinopyroxene and amphibole influence trace element incorporation into the sodic Fe–Mg silicates (Blundy *et al.*, 1995; Bennett *et al.*, 2004; Marks *et al.*, 2004*b*) although competition with coexisting HFSE-incorporating phases for REE [e.g. astrophyllite-group minerals: Piilonen *et al.*, 2000: eudialyte-group minerals (EGM): Schilling *et al.*, 2011*b*] may have an additional effect on the REE uptake into Fe–Mg silicates. Owing to the complex interplay between the crystal chemical effects of clinopyroxene and amphibole, locally variable concentrations of the REE in the various syenitic magmas and competition with numerous HFSE-incorporating minerals, such as the EGM, no definite conclusions can be drawn on the genetic relationship between the various foid syenites.

Ratios of selected trace elements also imply derivation from a common parent magma with fractionation from gabbros via diorites to syenites. Overlapping trace element ratios between the various units are observed for Zr/Hf, Nb/Ta, U/Th and Y/Ho in both clinopyroxene and amphibole (not shown). Even at variable concentrations of Zr, Hf, Nb, Ta, U, Th, Y and Ho most of the above element ratios remain constant in all units. Samples that are distinct in Zr/Hf, Nb/Ta, U/Th and/or Y/Ho contain Na–Fe^{3+}-rich clinopyroxene and amphibole that coexist with other HFSE minerals, with which they compete for HFSE.

To address the probable characteristics of the parental melt, we calculated the melt composition based on the REE composition of clinopyroxene in the least fractionated gabbroic unit using the partition coefficients of Zack & Brumm (1998; Fig. 18). The calculated melt composition closely resembles the OIB REE pattern of Sun & McDonough (1989) and overlaps with the REE patterns of whole-rocks from the New England Seamounts (Fig. 18), which we interpret to indicate derivation from a deep-seated hotspot, suggesting a common source for the Mont Saint-Hilaire and the New England Seamount chain. This interpretation is in agreement with the work of Eaton & Frederiksen (2007), who stated that the Monteregian Hills are part of the great Meteor hotspot track under North America and the adjacent Atlantic Ocean, based on seismic evidence.

Radiogenic and stable isotopes

Overlapping $\varepsilon_{Nd}(T = 125\ Ma)$ values from all units indicate either a common parental magma or at least a common source region for all the Mont Saint-Hilaire rock types; our data overlap with previously published ε_{Nd} values (Gilbert, 1985; Foland *et al.*, 1988; Fig. 11). The significant decrease in ε_{Nd} observed for the hydrothermal samples may point to increasing degrees of assimilation of crustal material during the late-stage evolution of the foid syenites (see below; Marks *et al.*, 2004*b*). Our ε_{Nd} data are in agreement with the interpretation of Greenwood & Edgar (1984) and the conclusion of Gilbert & Foland (1986), who stated that, based on field evidence and the overlapping ages of all rock units, the various Mont Saint-Hilaire lithologies are co-magmatic.

The $\delta^{18}O$ values of the Fe–Mg silicates are typical of mantle values (e.g. Kyser, 1986; Mattey *et al.*, 1994; Eiler, 2001; Marks *et al.*, 2004*b*, and references therein; Fig. 12). Slightly differing $\delta^{18}O$ values for some texturally and compositionally similar clinopyroxenes and amphiboles found within each (sub-)unit indicate disequilibrium conditions with respect to stable oxygen isotopes. The biotite and olivine oxygen isotope compositions invariably imply higher $\delta^{18}O$ melt values than do clinopyroxene and amphiboles. Hence, we interpret biotite and olivine to have re-equilibrated to higher degrees than clinopyroxene and amphibole.

We calculated oxygen isotope compositions for the coexisting melt by combining the mineral–water and rock–water fractionation coefficients of Zheng (1993*a*, 1993b) and Zhao & Zheng (2003), respectively. In accordance with the variable $\delta^{18}O$ values of the various mineral

separates, the calculated oxygen isotope compositions of the melts (at an assumed temperature of 1000°C) vary between 4·6 and 7·9‰ for all units, with the majority of samples falling close to typical mantle values of between 5·5 and 6‰ determined for basalts (e.g. Ito *et al.*, 1987; Eiler, 2001).

The hydrogen isotopic compositions of amphibole and biotite are similar to the δD values of hydrosilicates from other mantle-derived alkaline rocks, although lower δD values have been reported for the Ilímaussaq intrusion in Greenland (e.g. Marks *et al.*, 2004*b*; Waczek, 2009, and references therein; Fig. 13). No systematic variation is observed from gabbros to syenites with respect to hydrogen and oxygen isotopic composition, and Δamp–bt values are different even for mineral pairs that are similar in major element composition. Furthermore, hydrogen isotopes are prone to re-equilibration and structurally different minerals have different closure temperatures for hydrogen exchange (e.g. Taylor, 1974; Graham *et al.*, 1984; Huebner *et al.*, 1986; Brandriss *et al.*, 1995). This is in agreement with hydrothermal alteration and related fluid activity, as indicated by fluid inclusions, late-stage mineral equilibria and the stable isotope compositions of the late-stage minerals (see below).

The post-magmatic to hydrothermal stage: formation of late-stage mineral associations

Intensive parameters in the hydrothermal stage

As some of the stable oxygen isotope and fluid inclusion data point to extensive hydrothermal activity, we calculated activity–activity diagrams to investigate sub-solidus phase relations. In the late-stage assemblages of the syenites Na–Al silicates constrain the intensive parameters. Phase equilibria between nepheline$_{ss}$, the albite component in feldspar, natrolite, analcime and Na-chabazite allow estimation of the activities of SiO_2 and water at fixed pressure and temperature. As clinopyroxene in the late-stage assemblages approaches the pure aegirine end-member in composition and jadeite is virtually absent as a component, we ignored the latter in our calculations. Following the approaches of, for example, Liou (1971), Chipera & Apps (2001), Markl & Baumgartner (2002) and Weisenberger & Bucher (2010), we calculated a_{SiO2} vs a_{H2O} diagrams based on the following equilibria for temperature estimates based on oxygen isotope thermometry of the late-stage assemblages involving carbonates and some of the minerals and mineral assemblages considered in the following reactions:

$$NaAlSiO_4\ (Nph) + 2SiO_2\ (fluid) = NaAlSi_3\ O_8 (Ab) \quad (5)$$

$$NaAlSiO_4\ (Nph) + SiO_2\ (fluid) + H_2O\ (fluid) = NaAlSi_2O_6xH_2O (Anl) \quad (6)$$

$$2NaAlSiO_4\ (Nph) + SiO_2\ (fluid) + 2H_2O\ (fluid) = Na_2Al_2Si_3O_{10}x2H_2O\ (Ntr) \quad (7)$$

$$2NaAlSiO_4\ (Nph) + 2SiO_2\ (fluid) + 6H_2O\ (fluid) = Na_2Al_2Si_4O_{12}x6H_2O\ (Cbz) \quad (8)$$

$$NaAlSi_3O_8\ (Ab) + H_2O\ (fluid) = NaAlSi_2O_6xH_2O\ (Anl) + SiO_2 (fluid) \quad (9)$$

$$2NaAlSi_3O_8\ (Ab) + 2H_2O\ (fluid) = Na_2Al_2Si_3O_{10}x2H_2O\ (Ntr) + 3SiO_2\ (fluid) \quad (10)$$

$$2NaAlSi_3O_8\ (Ab) + 6H_2O\ (fluid) = Na_2Al_2Si_4O_{12}x6H_2O\ (Cbz) + 2SiO_2\ (fluid) \quad (11)$$

$$2NaAlSi_2O_6.H_2O\ (Anl) = Na_2Al_2Si_3O_{10}x2H_2O\ (Ntr) + SiO_2\ (fluid) \quad (12)$$

$$2NaAlSi_2O_6xH_2O\ (Anl) + 4H_2O\ (fluid) = Na_2Al_2Si_4O_{12}x6H_2O\ (Cbz) \quad (13)$$

$$Na_2Al_2Si_3O_{10}.2H_2O\ (Ntr) + SiO_2\ (fluid) + 4H_2O\ (fluid) = Na_2Al_2Si_4O_{12}x6H_2O\ (Cbz). \quad (14)$$

For nepheline, we used a one-site mixing model and, as a result of minor compositional variation, averaged analyses. For albite, natrolite and analcime we used unit activities owing to their near-endmember compositions. As no thermodynamic data for Na-chabazite are available, we constructed a qualitative μ_{SiO2}–μ_{H2O} diagram involving Na-chabazite to show the correct chemographic relationship with the above-mentioned minerals (Fig. 19a) but calculated quantitative diagrams without Na-chabazite (Fig. 19b–d). For calculation of the quantitative a_{SiO2}–a_{H2O} diagrams, we used the Unitherm database from the HCh package (Shvarov & Bastrakov, 1999; Shvarov, 1999) and the thermodynamic data of Holland & Powell (1998) for albite and nepheline and those of Robie & Hemingway (1995) with the Cp coefficients of Berman & Brown (1985) for natrolite. We applied the revised HKF model of Shock & Helgeson (1988) for SiO_2 and the HCh Unitherm-implemented calibration for H_2O. The accuracy of our estimates depends on the consistency of the thermodynamic data available. The thermodynamic data for nepheline, albite and analcime are internally consistent, whereas the thermodynamic data for natrolite are not consistent with those of the above minerals. This, however, does not affect the general conclusions drawn based on our estimates.

At 250°C, nepheline of the analyzed composition and pure albite buffer a_{SiO2} to equilibrium values of ~0·001 and at $a_{H2O} > \sim 0{\cdot}08$, natrolite becomes stable as the only zeolite mineral. Equilibrium (10) buffers a_{SiO2} to higher values than equation (5) (Nph–Ab) whereas equation (7) buffers a_{SiO2} to lower values than equation (5) (Fig. 19b).

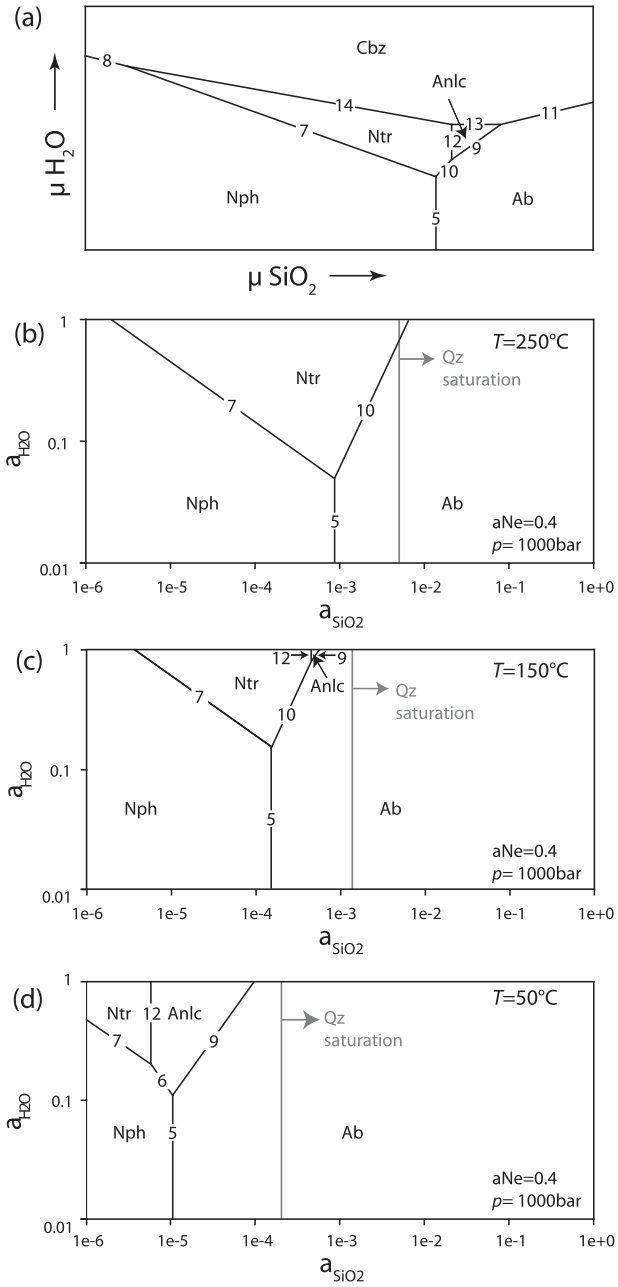

Fig. 19. (a) Qualitative μ–μ diagram showing the stability fields of the Na–Al silicates discussed in the text; (b–d) quantitative a_{SiO2}–a_{H2O} diagrams for selected Na–Al silicates at different temperatures. Grey lines represent the lower limits of quartz saturation. All diagrams are calculated at 1 kbar pressure; reaction numbers are as in the text.

At 150°C, analcime becomes stable at the expense of natrolite at the high-a_{SiO2} limit of the natrolite stability field, and nepheline and albite buffer a_{SiO2} to equilibrium values of the order of ~0·0001 (Fig. 19c). At 50°C, analcime is the major zeolite stable at elevated a_{H2O}, and a_{SiO2} is buffered to values between 0·0001 and 0·000001 by the various SiO_2-consuming reactions (Fig. 19d).

The phase relations in Fig. 19 show the stability fields for the zeolite minerals relevant at Mont Saint-Hilaire (compare, for example, with Liou, 1971, 1979; Chipera & Apps, 2001, and references therein; Markl & Baumgartner, 2002; Mitchell & Liferovich, 2006; Renac *et al.*, 2010). Calculated saturation of quartz for the respective conditions plots at higher silica activities than the observed phase equilibria that buffer the activities of water and SiO_2; this is in agreement with the absence of quartz in the late-stage assemblages used for calculating Fig. 19. At the temperatures chosen for our phase diagrams, hydrothermal fluids from other localities (even those that coexist with quartz-bearing lithologies) were found to dissolve similarly small amounts of SiO_2 (e.g. Pauwels *et al.*, 1993; Sanjuan *et al.*, 2010) and conversion of these concentration data for dissolved SiO_2 into SiO_2 activities, assuming equilibrium conditions, reveals silica activities in the same range as that calculated based on the late-stage Na–Al silicates in our syenites.

Although analcime is known to occur under a wide range of hydrothermal conditions in nature (e.g. Liou, 1971), it is stable only at temperatures ≤150°C (Fig. 19b and c). The calculated phase stabilities, however, are in agreement with the specific situation found at Mont Saint-Hilaire and the common observation of analcime pseudomorphs after natrolite in late-stage mineral assemblages.

Carbonate–carbonate and carbonate–silicate equilibria provide further constraints on temperature based on oxygen isotope composition. Using the fractionation coefficients of Zheng (1993*a*, 1999) indicates temperatures between 380°C (±200°C) and 80°C (±40°C).

Provenance of the late-stage fluids

The carbon and oxygen isotope compositions of carbonates can be used to determine the source characteristics of the fluids. Late-stage carbonates from the syenites isotopically resemble the limestone host-rocks of the intrusion or plot between limestone and typical mantle carbonate compositions (e.g. Taylor *et al.*, 1967; Fig. 14). This argues for the contribution of two sources to the carbon and oxygen incorporated into the carbonates: first, a magmatic component predominates in most siderite, rhodochrosite, dolomite, and some other carbonates. Second, a component that isotopically resembles the surrounding St. Lawrence Lowlands limestones predominates in texturally late calcite and siderite. Calcite from a coarse-grained marble xenolith has preserved its C and O isotopic composition, which overlaps with the St. Lawrence limestone data of Carignan *et al.* (1997) and late-stage dawsonite and calcite from a Monteregian feldspathic dike (Boussaroque *et al.*, 1975). Some calcites fall off the mixing line between the mantle and limestone reservoirs and trend towards the

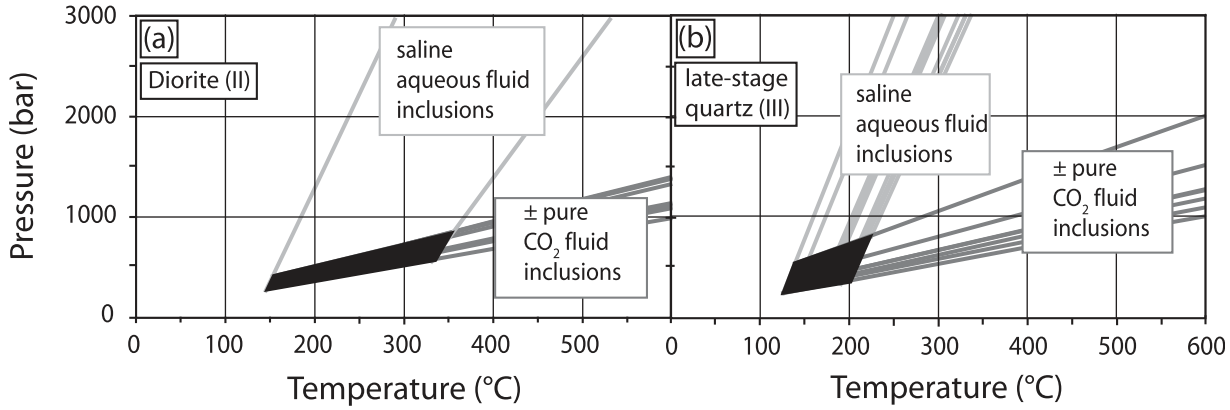

Fig. 20. Calculated isochors for coexisting (cogenetic) group (a) carbonic and group (b) aqueous fluid inclusions found within single trails. (a) Diorites; (b) late-stage quartz. The intersecting fields (dark) are interpreted to represent the trapping conditions for both fluid inclusion types.

isotopic composition of CO_2 extracted from fluid inclusions in a late-stage cryolite with low $\delta^{13}C$ and elevated $\delta^{18}O$ values. A potential source for this (relatively low $\delta^{13}C$) isotopic composition could be dissolved organic matter, which generally is thermally altered around intrusions in the St. Lawrence Lowlands (Héroux & Tassé, 1990). Hence, C and O from organic matter are likely to have been mobilized and introduced into the syenites during the emplacement of the Mont Saint-Hilaire intrusion. This is in agreement with the presence of rare graphite in late-stage assemblages.

Fluid inclusion data complement those of the carbonate stable isotope characteristics and the ε_{Nd} data for the hydrothermal samples, and reflect the complex late-stage history of Mont Saint-Hilaire. The formation of the fluid inclusions in the various Mont Saint-Hilaire lithologies is related to at least two events. We interpret the secondary aqueous group (b) fluid inclusions that are not cogenetic with carbonic group (a) fluid inclusions to have been trapped from an aqueous fluid that unmixed from the crystallizing and cooling magma in the late-magmatic and/or subsequent hydrothermal stage. Such a process has been reported to account for the formation of aqueous fluid inclusions in numerous alkaline rock occurrences (e.g. Tamazeght: Salvi *et al.*, 2000; Ditrau: Fall *et al.*, 2007; Ilímaussaq: Graser *et al.*, 2008; Ivigtut: Köhler *et al.*, 2008) and may be supported by the relatively high homogenization temperatures of some of the aqueous fluid inclusions found in the foid syenites. Large variations observed in the final melting and homogenization temperatures of such fluid inclusions may point to mixing with variable proportions of an external fluid (Fig. 16b). The absence or scarcity of hydrocarbons in our fluid inclusions might indicate more oxidized (late-) magmatic conditions than, for example, at Ilímaussaq (Krumrei *et al.*, 2007; Graser *et al.*, 2008; Markl *et al.*, 2010) or Khibina (Beeskow *et al.*, 2006).

We interpret the formation of secondary trails consisting of carbonic group (a) and aqueous group (b) fluid inclusions to be related to heterogeneous trapping of an externally derived immiscibly coexisting CO_2–H_2O fluid. Owing to the different wetting behavior of H_2O and CO_2 (e.g. Hollister, 1990; Belkin & De Vivo, 1993), the relative amounts of group (a) and (b) fluid inclusions cannot be assumed to represent the composition of the immiscibly coexisting fluid. However, the presence of cogenetic carbonic and aqueous fluid inclusions allows us to constrain the conditions of capture of the fluids: calculated isochors (MacFlincCor; Brown & Hagemann, 1995) for cogenetic group (a) and (b) fluid inclusions intersect between ~350°C at ~0·8 kbar and ~150°C at ~0·3 kbar in nepheline (in a dioritic sample) and between 230°C at ~0·7 kbar and 130°C at ~0·3 kbar in late-stage quartz (Fig. 20). Both nepheline and quartz can be assumed to represent relatively stable containers for fluid inclusions, which prevents post-entrapment modification of the fluid inclusions. The *P*–*T* conditions indicated by intersections of the isochors (Fig. 20) are in good agreement with experimental studies on the H_2O–CO_2 solvus, which lies at ~265°C for the pure system (e.g. Tödheide & Franck, 1963; Diamond, 2001) and is shifted towards higher temperatures if NaCl is added to the system (Hendel & Hollister, 1981; Bowers & Helgeson, 1983). Hence, percolation of an immiscibly coexisting external CO_2-rich and saline aqueous fluid, probably in equilibrium with limestone country-rocks, is interpreted to have affected all rock units. This interpretation is supported by the stable isotope compositions of CO_2 from fluid inclusions in diorite, which isotopically overlap with those of limestones (Fig. 14). We interpret the relatively homogeneous final melting temperatures at variable homogenization temperatures observed in the late-stage quartz (Fig. 16b) to reflect cooling of the externally derived fluid, which points to long-lived hydrothermal activity controlled by external fluids. To conclude,

infiltration of an externally derived, immiscibly coexisting CO_2–H_2O fluid has the potential to form both CO_2 and aqueous fluid inclusions, to stabilize carbonate minerals intergrown with late-stage silicates, and to control the C and O stable isotope composition of carbonate minerals and the CO_2 in fluid inclusions. Alternatively, partial melting of marble xenoliths, as described by McDonald & Chao (2004), could account for these observations; however, based on the small volumes of recrystallized rather than partially dissolved marble xenoliths observed in outcrop, partial melting of marble xenoliths appears only to co-contribute to the infiltration of external fluids. The latter process may locally predominate over the former.

The results of our study of late-stage mineral assemblages imply similar potential for late-stage mineral formation in other alkaline complexes emplaced into limestones (e.g. Saima: Saima Deposit Research Group, 1987; Tamazeght: Allah *et al.*, 1998).

SUMMARY AND CONCLUSIONS

Our investigation of the magmatic to hydrothermal evolution of Mont Saint-Hilaire yields the following results.

(1) Trace element and REE data together with oxygen, hydrogen and Nd isotopic data for Fe–Mg silicates indicate a common mantle-derived parent magma with OIB characteristics for the major Mont Saint-Hilaire lithologies and underline the importance of fractional crystallization during the magmatic evolution of the complex. For some of the evolved syenites, however, increasing degrees of crustal contamination are implied.

(2) Calculated silica activities vary strongly (0·7–0·3) in gabbros; samples indicating temperatures <800°C display the widest range in a_{SiO2}, arguing for late-magmatic to subsolidus re-equilibration. Silica activity is relatively homogeneous (0·4–0·5) in diorites and we estimate values of $a_{SiO2}=0{\cdot}6$ at near-liquidus conditions and values around of $a_{SiO2}=0{\cdot}3$ in the late-magmatic stage in the syenites. With the transition of late-magmatic to hydrothermal conditions, a_{SiO2} drops to values around ~0·001, which is due to lower SiO_2 solubilities in aqueous fluids compared with silicate melts and to decreasing temperature.

(3) Oxygen fugacity in the early magmatic gabbroic rocks varies between $\Delta FMQ=-0{\cdot}5$ and $+0{\cdot}7$ (at 1200 to 900°C) and increases to values around $\Delta FMQ=+2$ in the late- to post-magmatic stage. In diorites, f_{O2} is confined to values around $\Delta FMQ=-1$ and hence this unit crystallized under lower oxygen fugacities. Especially the diorites provide evidence that low silica activity drives oxygen fugacity to lower values as indicated by QUIlF-type equilibria involving nepheline and feldspar in the diorites (Schilling *et al.*, 2011*a*); this is supported by numerous studies of silica-undersaturated systems, which show that these magmatic systems have great potential to crystallize under reduced conditions (e.g. Markl *et al.*, 2010).

(4) Late-stage assemblages involving carbonates and Na–Al silicates have equilibrated at temperatures <400°C and reflect the provenance of late-stage fluids from two sources. First, a magmatic component is present as an exsolved magmatic fluid phase that isotopically represents a mantle component. Second, external fluids probably in equilibrium with the surrounding sedimentary host-rocks contribute to the oxygen and carbon isotopic compositions of carbonates, indicating that external fluids have infiltrated the intrusive body. Locally, partial melting of marble xenoliths may contribute to the oxygen and carbon stable isotopic composition.

(5) Fluid inclusions record an aqueous fluid that probably exsolved from the residual magma. Subsequently, external aqueous fluids infiltrated the intrusive body and were trapped in the course of a heterogeneous trapping process. This externally derived, immiscibly coexisting CO_2–H_2O fluid was trapped at temperatures <340°C in all units.

(6) The combination of different processes contributed to the formation of the mineral wealth found at Mont Saint-Hilaire: first, magmatic pre-enrichment of alkalis, LILE and HFSE; second, mixing of an exsolved magmatic fluid with external fluids; third, low-temperature fluid–rock interaction resulted in dissolution, transport and re-precipitation of characteristic mineral assemblages dependent on locally variable parameters.

(7) Emplacement of the silicate intrusive rocks into limestone host-rocks plays a key role in the formation of the large mineralogical diversity found at Mont Saint-Hilaire. Owing to extreme chemical gradients between the limestone host-rocks and the emplaced silicate magmas there are strong temporal and spatial variations in the intensive parameters, which locally favor specific phase assemblages. Thus, other alkaline complexes emplaced into limestone host-rocks (Saima: Saima Deposit Research Group, 1987; Tamazeght: Allah *et al.*, 1998), have a similarly high potential to develop exotic and elsewhere rare minerals.

ACKNOWLEDGEMENTS

B. Walter was of invaluable help with mineral separation for isotope analyses. G. Stoschek, E. Reitter and B. Steinhilber are thanked for their help with the isotope analysis. M. Keuper helped with Raman spectroscopy of fluid inclusions, and N. Huber helped with X-ray diffraction. I. Gill-Kopp is thanked for sample preparation.

T. Fußwinkel, K. Pfaff and K. Hettmann are thanked for insightful discussions. McGill University is thanked for the collaboration and sampling permission in the Gault Nature Reserve, Mont Saint-Hilaire. The Canadian Museum of Nature (Ottawa) kindly provided sample material from late-stage associations. Comments from the reviewers R. Mitchell, T. Andersen and P. Piilonen, and the editor M. Wilson, substantially improved the quality of the paper.

FUNDING

Financial support from the Deutsche Forschungsgemeinschaft (grant MA 2135/12) is gratefully acknowledged.

SUPPLEMENTARY DATA

Supplementary data for this paper are available at *Journal of Petrology* online.

REFERENCES

Adams, F. D. (1903). The Monteregian Hills: a Canadian Petrographical Province. *Journal of Geology* **11**, 239–282.

Allah, B. K., Fontan, F., Kadar, M., Monchoux, P. & Sørensen, H. (1998). Reactions between agpaitic nepheline syenitic melts and sedimentary carbonate rocks, exemplified by the Tamazeght Complex, Morocco. *Geochemistry International* **36**, 569–581.

Allan, J. F. (1992). Geology and mineralization of the Kipawa Yttrium–Zirconium prospect, Quebec. *Exploration and Mining Geology* **1**, 283–295.

Andersen, D. J., Lindsley, D. H. & Davidson, P. M. (1993). QUILF: a PASCAL program to assess equilibria among Fe–Mg–Ti oxides, pyroxenes, olivine and quartz. *Computers and Geosciences* **19**, 1333–1350.

Andersen, T., Erambert, M., Larsen, A. O. & Selbekk, R. S. (2010). Petrology of nepheline syenite pegmatites in the Oslo rift, Norway: zirconium silicate mineral assemblages as indicators of alkalinity and volatile fugacity in mildly agpaitic magma. *Journal of Petrology* **51**, 2303–2325.

Armstrong, J. T. (1991). *Quantitative Elemental Analysis of Individual Microparticles with Electron Beam Instruments*. New York: Plenum.

Bailey, J. C., Bohse, H., Gwozdz, R. & Rose-Hansen, J. (1993). Li in minerals from the Ilímaussaq alkaline intrusion, South Greenland. *Bulletin of the Geological Society of Denmark* **40**, 288–299.

Beeskow, B., Treloar, P. J., Rankin, A. H., Vennemann, T. & Spangenberg, J. (2006). A reassessment of models for hydrocarbon generation in the Khibina Mountains, NW Russia. *Lithos* **91**, 1–18.

Belkin, H. E. & De Vivo, B. (1993). Fluid inclusion studies of ejected nodules from Plinian eruptions of Mt. Somma–Vesuvius. *Journal of Volcanology and Geothermal Research* **58**, 89–100.

Bennett, S. L., Blundy, J. & Elliott, T. (2004). The effect of sodium and titanium on crystal–melt partitioning of trace elements. *Geochimica et Cosmochimica Acta* **68**, 2335–2347.

Berman, R. (1988). Internally consistent thermodynamic data for minerals in the system Na_2O–K_2O–CaO–MgO–FeO–Fe_2O_3–Al_2O_3–SiO_2–H_2O–CO_2. *Journal of Petrology* **29**, 445–522.

Berman, R. & Brown, T. H. (1985). Heat capacity of minerals in the system Na_2O–K_2O–CaO–MgO–FeO–Fe_2O_3–Al_2O_3–SiO_2–TiO_2–H_2O–CO_2: representation, estimation, and high temperature extrapolation. *Contributions to Mineralogy and Petrology* **89**, 168–183.

Berman, R. G., Brown, T. H. & Perkins, E. H. (1987). Geo-Calc; a software for calculation and display of *P–T–X* phase diagrams. *American Mineralogist* **72**, 861–862.

Bindeman, I. & Davis, A. (2000). Trace element partitioning between plagioclase and melt: Investigation of dopant influence on partition behavior. *Geochimica et Cosmochimica Acta* **64**, 2863–2878.

Blundy, J. D., Falloon, T. J., Wood, B. J. & Dalton, J. A. (1995). Sodium partitioning between clinopyroxene and silicate melts. *Journal of Geophysical Research* **100**, 15501–15515.

Bodnar, R. J. (1993). Revised equation and table for determining the freezing point depression of H_2O–NaCl solutions. *Geochimica et Cosmochimica Acta* **57**, 683–684.

Boily, M. & Williams-Jones, A. E. (1994). The role of magmatic and hydrothermal processes in the chemical evolution of the Strange Lake plutonic complex, Québec–Labrador. *Contributions to Mineralogy and Petrology* **118**, 33–47.

Boussaroque, J.-L., Létolle, R. & Maury, R. A. (1975). Formation de la dawsonite des Richât (Adrar de Mauritanie) analyse isotopique ^{13}C et ^{18}O. *Comptes Rendus de l'Académie des Sciences, Série D* **281**, 1075–1078.

Bowers, T. S. & Helgeson, H. C. (1983). Calculation of the thermodynamic and geochemical consequences of nonideal mixing in the system H_2O–CO_2–NaCl on phase relations in geologic systems: Equation of state for H_2O–CO_2–NaCl fluids at high pressures and temperatures. *Geochimica et Cosmochimica Acta* **47**, 1247–1275.

Brandriss, M. E., Nevle, R. J., Bird, D. K. & O'Neil, J. R. (1995). Imprint of meteoric water on the stable isotope compositions of igneous and secondary minerals, Kap Edvard Holm complex, East Greenland. *Contributions to Mineralogy and Petrology* **121**, 74–86.

Brown, P. E. & Hagemann, S. G. (1995). Macflincor and its application to fluids in Archean lode-gold deposits. *Geochimica et Cosmochimica Acta* **59**, 3943–3952.

Carignan, J., Gariépy, C. & Hillaire-Marcel, C. (1997). Hydrothermal fluids during Mesozoic reactivation of the St. Lawrence rift system, Canada: C, O, Sr and Pb isotopic characterization. *Chemical Geology* **137**, 1–21.

Chakhmouradian, A. R., Halden, N. M., Mitchell, R. H. & Horváth, L. (2007). Rb–Cs-rich rasvumite and sector-zoned 'loparite-(Ce)' from Mont Saint-Hilaire (Québec, Canada) and their petrologic significance. *Eutopean Journal of Mineralogy* **19**, 533–546.

Chao, G. Y., Harris, D. C., Hounslow, A. W., Mandarino, J. A. & Perrault, G. (1967). Minerals from the nepheline syenite, Mont St. Hilaire, Quebec. *Canadian Mineralogist* **9**, 109–123.

Chipera, S. J. & Apps, J. A. (2001). Geochemical stability of natural zeolites. In: Bish, D. & Ming, D. (eds) *Natural Zeolites: Occurrence, Properties, Applications. Mineralogical Society of America and Geochemical Society, Reviews in Mineralogy and Geochemistry* **45**, 117–161.

Coulson, I. A. (1997). Post-magmatic alteration in eudialyte from the North Qôroq centre, South Greenland. *Mineralogical Magazine* **61**, 99–109.

Coulson, I. M. (2003). Evolution of the North Qôroq centre nepheline syenites, South Greenland: alkali–mafic silicates and the role of metasomatism. *Mineralogical Magazine* **67**, 873–892.

Craig, H. (1961). Standards for reporting concentrations of deuterium and oxygen 18 in natural waters. *Science* **133**, 1833–1834.

Currie, K. L. (1989). *Geology and Composition of the Mont Saint-Hilaire Pluton, Southern Québec. Geological Survey of Canada Open File* **2031**, 35 p.

Currie, K. L., Eby, G. N. & Gittins, J. (1986). The petrology of the Mont Saint-Hilaire complex, southern Quebec: an alkaline gabbro–peralkaline syenite association. *Lithos* **19**, 65–81.

Diamond, L. W. (2001). Review of the systematics of H_2O–CO_2 fluid inclusions. *Lithos* **55**, 69–99.

Eaton, D. W. & Frederiksen, A. (2007). Seismic evidence for convection-driven motion of the North American plate. *Nature* **446**, 428–431.

Eby, G. N. (1985). Sr and Pb isotopes, U and Th chemistry of the alkaline Monteregian and White Mountain igneous provinces, eastern North America. *Geochimica et Cosmochimica Acta* **49**, 1143–1153.

Eiler, J. M. (2001). Oxygen isotope variations of basaltic lavas and upper mantle rocks. In: Valley, J. W. & Cole, D. (eds) *Stable Isotope Geochemistry. Mineralogical Society of America and Geochemical Society, Reviews in Mineralogy and Geochemistry* **43**, 319–364.

Fall, A., Bodnar, R. J., Csaba, S. & Pál-Molnár, E. (2007). Fluid evolution in the nepheline syenites of the Ditrau Alkaline Massif, Transylvania, Romania. *Lithos* **95**, 331–345.

Foland, K. A., Jiang-feng, C., Gilbert, L. A. & Hofmann, A. W. (1988). Nd and Sr isotopic signatures of Mesozoic plutons in northeastern North America. *Geology* **16**, 684–687.

Friedman, I. (1953). Deuterium content of natural waters and other substances. *Geochimica et Cosmochimica Acta* **4**, 89–103.

Frost, B. R., Lindsley, D. H. & Andersen, D. J. (1988). Fe–Ti oxide–silicate equilibria: Assemblages with fayalitic olivine. *American Mineralogist* **73**, 727–740.

Fuhrman, M. L. & Lindsley, D. H. (1988). Ternary-feldspar modeling and thermometry. *American Mineralogist* **73**, 201–215.

Gilbert, L. A. (1985). Petrogenesis of the Mont St. Hilaire alkaline igneous complex, Quebec. MS thesis, Ohio State University, Columbus, 262 pp.

Gilbert, L. A. & Foland, K. A. (1986). The Mont Saint Hilaire plutonic complex: occurrence of excess ^{40}Ar and short intrusion history. *Canadian Journal of Earth Sciences* **23**, 948–958.

Gold, D. P. (1963). The relationship between the limestones and the alkaline igneous rocks of Oka and St. Hilaire, Quebec. PhD thesis, McGill University, Montreal, 354 pp.

Gold, D. P. (1967). Alkaline ultrabasic rocks in the Montreal area, Quebec. In: Wyllie, P. J. (ed.) *Ultramafic and Related Rocks*. New York: Wiley, pp. 288–302.

Graham, C. M., Harmon, R. S. & Sheppard, S. M. F. (1984). Experimental hydrogen isotope studies: hydrogen isotope exchange between amphibole and water. *American Mineralogist* **69**, 128–138.

Graser, G. & Markl, G. (2008). Ca-rich ilvaite–epidote–hydrogarnet endoskarns: a record of late-magmatic fluid influx into the persodic Ilímaussaq Complex, South Greenland. *Journal of Petrology* **49**, 239–265.

Graser, G., Potter, J., Köhler, J. & Markl, G. (2008). Isotope, major, minor and trace element geochemistry of late-magmatic fluids in the peralkaline Ilímaussaq intrusion, South Greenland. *Lithos* **106**, 207–221.

Greenwood, R C. & Edgar, A. D. (1984). Petrogenesis of the gabbros from Mt St. Hilaire, Quebec, Canada. *Geological Journal* **19**, 353–376.

Griffin, W. L., Powell, W. J., Pearson, N. J. & O'Reilly, S. Y. (2008). *GLITTER: Data reduction software for laser ablation ICP-MS*. Mineralogical Association of Canada, Short Course Series (appendix), Vol. 40, pp. 308–311.

Hamilton, D. L. (1961). Nephelines as crystallisation temperature indicators. *Journal of Geology* **69**, 321–329.

Hendel, E. M. & Hollister, L. S. (1981). An empirical solvus for CO_2–H_2O–2·6 wt % salt. *Geochimica et Cosmochimica Acta* **45**, 225–228.

Héroux, Y. & Tassé, N. (1990). Organic-matter alteration in an early Paleozoic basin: Zonation around mineral showings compared to that around intrusions, St. Lawrence Lowlands, Quebec, Canada. *Geological Society of America Bulletin* **102**, 877–888.

Holland, T. & Powell, R. (1998). An internally consistent thermodynamic data set for phases of petrological interest. *Journal of Metamorphic Geology* **16**, 309–343.

Holland, T. & Powell, R. (2003). Activity–composition relations for phases in petrological calculations: an asymmetric multicomponent formulation. *Contributions to Mineralogy and Petrology* **145**, 492–501.

Hollister, L. S. (1990). Enrichment of CO_2 in fluid inclusions in quartz by removal of H_2O during crystal-plastic deformation. *Journal of Structural Geology* **12**, 895–901.

Horváth, L. & Gault, R. A. (1990). The mineralogy of Mont Saint-Hilaire, Quebec. *Mineralogical Record* **21**, 284–392.

Huebner, M., Kyser, T. K. & Nosbet, E. G. (1986). Stable-isotope geochemistry of high-grade metapelites from the Central zone of the Limpopo belt. *American Mineralogist* **71**, 1343–1353.

Ito, E., White, W. M. & Göpel, C. (1987). The O, Sr, Nd, and Pb isotope geochemistry of MORB. *Chemical Geology* **62**, 157–176.

Jacob, D. E. (2006). High sensitivity analysis of trace element poor geological reference glasses by laser-ablation inductively coupled plasma mass spectrometry (LA-ICP-MS). *Geostandards and Geoanalytical Research* **30**, 221–235.

Jochum, K. P. & Nohl, U. (2008). Reference materials in geochemistry and environmental research and the GeoReM database. *Chemical Geology* **253**, 50–53.

Kogarko, L. N. (1990). Ore-forming potential of alkaline magmas. *Lithos* **26**, 167–175.

Kogarko, L. N., Lazutkina, L. N. & Romanchev, B. P. (1982). The origin of eudialyte mineralization. *Geochemistry International* **19**, 128–145.

Köhler, J., Konnerup-Madsen, J. & Markl, G. (2008). Fluid geochemistry in the Ivigtut cryolite deposit, South Greenland. *Lithos* **103**, 369–392.

Kramm, U. & Kogarko, L. N. (1994). Nd and Sr isotope signatures of the Khibina and Lovozero agpaitic centres, Kola Alkaline Province, Russia. *Lithos* **32**, 225–242.

Krumrei, T., Pernicka, E., Kaliwoda, M. & Markl, G. (2007). Volatiles in a peralkaline system: abiogenic hydrocarbons and F–Cl–Br systematics in the naujaite of the Ilímaussaq intrusion, South Greenland. *Lithos* **95**, 298–314.

Kyser, T. K. (1986). Stable isotope variations in the mantle. In: Valley, J. W., Taylor, H. P., Jr & O'Neil, J. R. (eds) *Stable Isotopes in High-Temperature Geological Processes. Mineralogical Society of America, Reviews in Mineralogy* **16**, 141–162.

Lalonde, A. E., Rancourt, D. G. & Chao, G. (1996). Fe-bearing trioctahedral micas from Mont Saint-Hilaire, Québec, Canada. *Mineralogical Magazine* **60**, 447–460.

Leake, B. E., Woolley, A. R. *et al.* (1997). Nomenclature of amphiboles: report of the subcommittee on amphiboles of the International Mineralogical Association, Commission on New Minerals and Mineral Names. *Canadian Mineralogist* **35**, 219–246.

Lemarchand, F., Benoit, V. & Calais, G. (1987). Trace element distribution coefficients in alkaline series. *Geochimica et Cosmochimica Acta* **51**, 1071–1081.

Liebermann, J. & Petrakakis, K. (1990). TWEEQU thermobarometry, analysis of uncertainties and applications to granulites from western Alaska. *Canadian Mineralogist* **29**, 857–887.

Liou, J. G. (1971). Analcime equilibria. *Lithos* **4**, 389–402.

Liou, J. G. (1979). Zeolite facies metamorphism of basaltic rocks from the East Taiwan Ophiolite. *American Mineralogist* **64**, 1–14.

Mann, U., Marks, M. & Markl, G. (2006). Influence of oxygen fugacity on mineral composition in peralkaline melts: The Katzenbuckel volcano, Southwest Germany. *Lithos* **91**, 262–285.

Markl, G. & Baumgartner, L. (2002). pH changes in peralkaline late-magmatic fluids. *Contributions to Mineralogy and Petrology* **144**, 331–346.

Markl, G., Marks, M., Schwinn, G. & Sommer, H. (2001). Phase equilibrium constraints on intensive crystallization parameters of the Ilímaussaq Complex, South Greenland. *Journal of Petrology* **42**, 2231–2258.

Markl, G., Marks, M. A. W. & Frost, B. R. (2010). On the controls of oxygen fugacity in the generation of peralkaline melts. *Journal of Petrology* **51**, 1831–1847.

Marks, M. & Markl, G. (2001). Fractionation and assimilation processes in the alkaline augite syenite unit of the Ilímaussaq Intrusion, South Greenland, as deduced from phase equilibria. *Journal of Petrology* **42**, 1947–1969.

Marks, M., Vennemann, T., Siebel, W. & Markl, G. (2003). Quantification of magmatic and hydrothermal processes in a peralkaline syenite–alkali granite complex based on textures, phase equilibria, and stable and radiogenic isotopes. *Journal of Petrology* **44**, 1247–1280.

Marks, M., Halama, R., Wenzel, T. & Markl, G. (2004*a*). Trace element variations in clinopyroxene and amphibole from alkaline to peralkaline syenites and granites: implications for mineral–melt trace-element partitioning. *Chemical Geology* **211**, 185–215.

Marks, M., Vennemann, T., Siebel, W. & Markl, G. (2004*b*). Nd-, O-, and H-isotopic evidence for complex, closed-system fluid evolution of the peralkaline Ilímaussaq intrusion, South Greenland. *Geochimica et Cosmochimica Acta* **68**, 3379–3395.

Marks, M. A. W., Hettmann, K., Schilling, J., Frost, B. R. & Markl, G. (2011). The mineralogical diversity of alkaline rocks: critical factors for the transition from miaskitic to agpaitic phase assemblages. *Journal of Petrology* **52**, 439–455.

Mattey, D., Lowry, D. & Macpherson, C. (1994). Oxygen isotope composition of mantle peridotite. *Earth and Planetary Science Letters* **128**, 231–241.

McCarthy, T. C. & Patiño Douce, A. E. (1998). Empirical calibration of the silica–Ca-Tschermak's–anorthite (SCAn) geobaromater. *Journal of Metamorphic Geology* **16**, 675–686.

McDonald, A. M. & Chao, G. Y. (2004). Haineaultite, a new hydrated sodium calcium titanosilicate from Mont Saint-Hilaire, Quebec: description, structure and genetic implications. *Canadian Mineralogist* **42**, 769–780.

Mitchell, R. H. (1990). A review of the compositional variation of amphiboles in alkaline plutonic complexes. *Lithos* **26**, 135–156.

Mitchell, R. H. & Liferovich, R. P. (2006). Subsolidus deuteric/hydrothermal alteration of eudialyte in lujavrite from the Pilansberg alkaline complex, South Africa. *Lithos* **91**, 352–372.

Mitchell, R. H. & Platt, R. G. (1978). Mafic mineralogy of ferroaugite syenite from the Coldwell alkaline complex, Ontario, Canada. *Journal of Petrology* **19**, 627–651.

O'Neill, J. J. (1914). *Saint-Hilaire (Beloeil) and Rougemont mountains, Quebec. Geological Survey of Canada Memoir* **43**, 108 p.

Palme, H. & O'Neill, H. S. C. (2004). Cosmochemical estimates on mantle composition. In: Carlson, R. W. (ed.) *Treatise on Geochemistry*. Amsterdam: Elsevier, pp. 1–38.

Paster, T. P., Schauwecker, D. S. & Haskin, L. A. (1974). The behavior of some trace elements during solidification of the Skaergaard layered series. *Geochimica et Cosmochimica Acta* **38**, 1549–1577.

Pauwels, H., Fouillac, C. & Fouillac, A.-M. (1993). Chemistry and isotopes of deep geothermal saline fluids in the Upper Rhine Graben: Origin of compounds and water–rock interactions. *Geochimica et Cosmochimica Acta* **57**, 2737–2749.

Philpotts, A. R. (1974). The Monteregian Province. In: Sørensen, H. (ed.) *The Alkaline Rocks*. New York: John Wiley, pp. 293–310.

Piilonen, P. C., McDonald, A. M. & Lalonde, A. E. (1998). The crystal chemistry of aegirine from Mont Saint-Hilaire, Quebec. *Canadian Mineralogist* **36**, 779–791.

Piilonen, P. C., Lalonde, A. E., McDonald, A. M. & Gault, R. A. (2000). Niobokupletskite, a new astrophyllite-group mineral from Mont Saint-Hilaire, Quebec, Canada: Description and crystal structure. *Canadian Mineralogist* **38**, 627–639.

Rajasekaran, K.C. (1967). Mineralogy and petrology of nepheline syenite in Mont St. Hilaire, Quebec. PhD thesis, McGill University, Montreal, 226 pp.

Renac, C., Kyser, K., Bowden, P., Moine, B. & Cottin, J.-Y. (2010). Hydrothermal fluid interaction in basaltic lava units, Kerguelen Archipelago (SW Indian Ocean). *European Journal of Mineralogy* **22**, 215–234.

Robie, A. & Hemingway, S. (1995). Thermodynamic properties of minerals and related substances at 298·15 K and 1 Bar (10^5 Pascals) pressure and at higher temperatures. *US Geological Survey Bulletin* **2131**, 1–461.

Rumble, D. & Hoering, T. C. (1994). Analysis of oxygen and sulfur isotope ratios in oxide and sulfide minerals by spot heating with carbon dioxide laser in a fluorine atmosphere. *Accounts of Chemical Research* **27**, 237–241.

Saima Deposit Research Group. (1987). Uranium deposit in the Saima alkaline massif, Northeast China. *Science Sinica* **21**, 365–389.

Salvi, S., Fontan, F., Monchoux, P., Williams-Jones, A. E. & Moine, B. (2000). Hydrothermal mobilization of High Field Strength Elements in alkaline igneous systems: evidence from the Tamazeght complex (Morocco). *Economic Geology* **95**, 559–576.

Sanjuan, B., Millot, R., Dezayes, C. & Brach, M. (2010). Main characteristics of the deep geothermal brine (5 km) at Soultz-sous-Forêts (France) determined using geochemical and tracer test data. *Comptes Rendus Géoscience* **342**, 546–559.

Schilling, J., Marks, M. A. W., Wenzel, T. & Markl, G. (2009). Reconstruction of magmatic to subsolidus processes in an agpaitic system using eudialyte textures and composition: a case study from Tamazeght, Morocco. *Canadian Mineralogist* **47**, 351–365.

Schilling, J., Frost, B. R., Marks, M. A. W., Wenzel, T. & Markl, G. (2011*a*). Fe–Ti oxide–silicate (QUILF-type) equilibria in feldspathoid-bearing systems. *American Mineralogist* **96**, 100–110.

Schilling, J., Wu, F.-Y., McCammon, C., Wenzel, T., Marks, M. A. W., Pfaff, K., Jacob, D. E. & Markl, G. (2011*b*). The compositional variability of eudialyte-group minerals (EGM). *Mineralogical Magazine* **75**, 87–115.

Schönenberger, J. & Markl, G. (2008). The magmatic and fluid evolution of the Motzfeldt Intrusion in South Greenland: insights into the formation of agpaitic and miaskitic rocks. *Journal of Petrology* **49**, 1549–1577.

Schumacher, J.C. (1997). The estimation of ferric iron in electron microprobe analysis of amphiboles. In: Leake, B.E. *et al.* (eds) *Nomenclature of Amphiboles: Report of the Subcommittee on Amphiboles of the International Mineral Association Commission on New Minerals and Mineral Names*, Mineralogical Magazine 61, Appendix 2, 312–321.

Sharp, Z. D. (1990). A laser-based microanalytical method for the *in situ* determination of oxygen isotope ratios of silicates and oxides. *Geochimica et Cosmochimica Acta* **54**, 1353–1357.

Sharp, Z. D., Atudorei, V. & Durakiewicz, T. (2001). A rapid method for determining the hydrogen and oxygen isotope ratios from water and solid hydrous substances. *Chemical Geology* **178**, 197–210.

Shock, E. L. & Helgeson, H. C. (1988). Calculation of the thermodynamic and transport properties of aqueous species at high pressures and temperatures: Correlation algorithms for ionic species and equation of state predictions to 5 kb and 1000°C. *Geochimica et Cosmochimica Acta* **52**, 2009–2036.

Shvarov, Y. V. (1999). Algorithmization of the numerical equilibrium modeling of dynamic geochemical processes. *Geochemistry International* **37**, 571–576.

Shvarov, Y. V. & Bastrakov, E. (1999). *HCh: A software package for geochemical equilibrium modeling. User's guide. Australian Geological Survey Organisation Record* **1999/25**, 61 p.

Sood, M. K. & Edgar, A. D. (1970). Melting relations of undersaturated alkaline rocks from the Ilímaussaq Intrusion and Gronnedal-Ika Complex, South Greenland, under water vapour and controlled partial oxygen pressures. *Meddelser om Grønland* **181**, 41 pp.

Sørensen, H. (1992). Agpaitic nepheline syenites: a potential source of rare minerals. *Applied Geochemistry* **7**, 417–427.

Sørensen, H. (1997). The agpaitic rocks—an overview. *Mineralogical Magazine* **61**, 485–498.

Sørensen, H., Danø, M. & Petersen, O. V. (1971). On the mineralogy and paragenesis of tugtupite $Na_8Al_2Be_2Si_8O_{24}(Cl,S)_2$ from the Ilímaussaq alkaline intrusion, South Greenland. *Bulletin Grønlands Geologiske Undersøgelse* **95**, 38 pp.

Spötl, C. & Vennemann, T. (2003). Continuous-flow isotope ratio mass spectrometric analysis of carbonate minerals. *Rapid Communications in Mass Spectrometry* **17**, 1004–1006.

Stansfield, J. (1923). Extensions of the Monteregian Petrological Province to the west and northwest. *Geological Magazine* **60**, 433–435.

Sun, S.-s. & McDonough, W. F. (1989). Chemical and isotopic systematics of oceanic basalts: implications for mantle composition and processes. In: Saunders, A. D. & Norry, M. J. (eds) *Magmatism in the Ocean Basins. Geological Society, London, Special Publications* **42**, 313–345.

Taras, B. D. & Hart, S. R. (1987). Geochemical evolution of the New England Seamount chain: isotopic and trace element constraints. *Chemical Geology* **64**, 35–54.

Taylor, H. P., Jr (1974). The application of oxygen and hydrogen isotope studies to problems of hydrothermal alteration and ore deposition. *Economic Geology* **69**, 843–883.

Taylor, H. P., Jr, Frechen, J. & Degens, E. T. (1967). Oxygen and carbon isotope studies of carbonatites from the Laacher See District, West Germany and the Alno District, Sweden. *Geochimica et Cosmochimica Acta* **31**, 407–430.

Tödheide, K. & Franck, E. U. (1963). Das Zweiphasengebiet und die kritische Kurve im System Kohlendioxid–Wasser bis zu Drucken von 3500 bar. *Zeitschrift für Physikalische Chemie* **37**, 387–401.

Ussing, N. V. (1912). *Geology of the country around Julianehaab, Greenland. Meddelser om Grønland* **38**, 426 p.

Vennemann, T. & O'Neil, J. R. (1993). A simple and inexpensive method of hydrogen isotope and water analysis of minerals and rocks based on zinc reagent. *Chemical Geology* **103**, 227–234.

Villemant, B., Jaffrezic, H., Joron, J. L. & Treuil, M. (1981). Distribution coefficients of major and trace elements—fractional crystallization in the alkali basalt series of Chaîne-des-Puys (Massif Central, France). *Geochimica et Cosmochimica Acta* **45**, 1997–2016.

Vuorinen, J. H., Hålenius, U., Whitehouse, M. J., Mansfeld, J. & Skelton, A. D. L. (2005). Compositional variations (major and trace elements) of clinopyroxene and Ti-andradite from pyroxenite, ijolite and nepheline syenite, Alnø Island, Sweden. *Lithos* **81**, 55–77.

Waczek, Z. (2009). Hydrogen isotope fractionations between amphiboles, micas, and fluids in alkaline igneous intrusions. PhD thesis, Université de Lausanne, 219 pp.

Weisenberger, T. & Bucher, K. (2010). Zeolites in fissures of granites and gneisses of the Central Alps. *Journal of Metamorphic Geology* **28**, 825–847.

Whitney, D. L. & Evans, B. W. (2010). Abbreviations for names of rock-forming minerals. *American Mineralogist* **95**, 185–187.

Wight, Q. & Chao, G. (1995). Mont Saint-Hiliare revisited. *Rocks and Minerals* **70**, 90–103, 131–138.

Workman, R. K. & Hart, S. R. (2005). Major and trace element composition of the depleted MORB mantle (DMM). *Earth and Planetary Science Letters* **231**, 53–72.

Zack, T. & Brumm, R. (1998). Ilmenite/liquid partition coefficients of 26 trace elements determined through ilmenite/clinopyroxene partitioning in garnet pyroxene. In: Gurney, J. J., Gurney, J. L., Pascoe, M. D. & Richardson, S. H. (eds) *Proceedings of the 7th International Kimberlite Conference*. Red Roof Design: Cape Town, pp. 986–988.

Zhao, Z.-F. & Zheng, Y.-F. (2003). Calculation of oxygen isotope fractionation in magmatic rocks. *Chemical Geology* **193**, 59–80.

Zheng, Y.-F. (1993*a*). Calculation of oxygen isotope fractionation in anhydrous silicate minerals. *Geochimica et Cosmochimica Acta* **57**, 1079–1091.

Zheng, Y.-F. (1993*b*). Calculation of oxygen isotope fractionation in hydroxyl-bearing silicates. *Earth and Planetary Science Letters* **120**, 247–263.

Zheng, Y.-F. (1999). Oxygen isotope fractionation in carbonate and sulfate minerals. *Geochemical Journal* **33**, 109–126.